Reconstruction of total grain size distribution of the climactic phase of a long-lasting eruption

Alfano, Fabrizio; Bonadonna, Costanza; Watt, Sebastian; Connor, Chuck; Volentik, Alain; Pyle, David

Link to publication on Research at Birmingham portal

1   **Reconstruction of total grain size distribution of the climactic phase of a long-lasting eruption: the**

2   **example of the 2008-2013 Chaitén eruption.**

3

4   Fabrizio Alfano[1], Costanza Bonadonna[2], Sebastian Watt[3], Chuck Connor[4], Alain Volentik[4#],

5   David M. Pyle[5]

6

7   1. School of Earth and Space exploration, Arizona State University, Tempe, AZ (USA)

8   2. Department of Earth Sciences, University of Geneva, Geneva (Switzerland)

9   3. School of Geography, Earth and Environmental Sciences, University oϕ Birmingham, Birmingham (U.K.)

10   4. University of South Florida, Tampa, FL (USA)

11   5. Department of Earth Sciences, University of Oxford (U.K.)

12   # Now at: ExxonMobil Exploration Company, Spring, TX (USA)

13

14   Corresponding Author:

15   Fabrizio Alfano

16   Arizona State University, School of Earth and Space Exploration

17   POBOX 876004

18   Tempe, AZ 85282-1404

19   email: fabrizio.alfano@asu.edu

20   Phone: 1-480-727-3578

21

22   Version: 17 May 2016

23

24   **Abstract**

25   The 2008-2013 eruption of Chaitén volcano (Chile), was a long-lasting eruption whose climactic

26   phase (May 6th 2008) produced a sub-Plinian plume, with height ranging between 14 to 20 km,

27   that dispersed to the NE, reaching the Atlantic coast of Argentina. The erupted material was

28   mainly of lithic origin (~77 wt%), resulting in a uni-modal Total Grain-Size Distribution (TGSD)

29   dominated by coarse ash (77 wt%), with Md_ϕ of 2.7 and σ_ϕ of 2.4. Lapilli clasts (> 2 mm)

30   dominate the proximal deposit within ~20 km of the vent, while coarse (63 μm - 2 mm) and fine

31   ash (<63 μm) sedimented as far as 800 km from vent, generating mostly poly-modal grain-size

32   distributions across the entire deposit. Given that most of the mass is sedimented in proximal

33   areas, results show that possible contributions of later explosive events to the thickness of the

34   distal deposit where layers are less distinguishable (>400 km) do not significantly affect the

35   determination of the TGSD. In contrast, gaps in data sampling in the medial deposit (in particular

36   the gap between 50 and 350 km from vent, that coincides with shifts in sedimentation regimes)

37   have large impacts on estimates of TGSD. Particle number distribution for this deposit is

38   characterized by a high power-law exponent (3.0) following a trend very similar to the vesicle

39   size distribution in the juvenile pyroclasts. Although this could be taken to indicate a bubble-

40   driven fragmentation process, we suggest that fragmentation was more likely the result of a

41   shear-driven process, because of the predominance of non-vesicular products (lithics and

42   obsidians) and the large fraction of coarse ash in the TGSD.

43

44   **Introduction**

45   Volcanic explosive eruptions inject large amounts of pyroclastic material into the atmosphere,

46   which is widely dispersed downwind from the volcano. The physical characteristics of the tephra

47 and of the associated deposits are closely related to the characteristics of volcanic eruptions that

48 produced them (e.g., magnitude and style of the eruption, plume dynamics and rise, conduit

49 dynamics and magma fragmentation). Therefore, a detailed study of individual pyroclasts and

50 associated deposits can provide critical insights into volcanic processes and can inform forecasts

51 of future eruptions (Houghton and Wilson 1989; Cashman and Mangan 1994; Bonadonna et al

52 2005; Bonadonna and Houghton 2005; Costantini et al 2010; Alfano et al 2011a; Rust and

53 Cashman 2011; Alfano et al 2012).

54 Volcanic particles originate from the fragmentation of fresh magma (juvenile clasts) and are

55 typically ejected from the eruptive vent together with lithic clasts, resulting from the disruption

56 of conduit and/or crater walls (Cas and Wright 1988). All clasts are injected into the atmosphere

57 and are transported laterally under the action of the spreading cloud and the prevailing winds,

58 and eventually sediment on the ground. Fallout processes mostly depend on particle size, with

59 the largest particles sedimenting rapidly, and the smallest particles remaining suspended in the

60 atmosphere for longer time periods, and sedimenting up to several hundreds of kilometres from

61 the vent (Watt et al 2009; Alfano et al 2011a; Durant et al 2012). As a result, the character of

62 tephra deposits varies significantly with the distance from the vent, as a function of plume height

63 and wind patterns (Walker 1971; Carey and Sparks 1986, Pyle, 1989).

64

65 Ideally, the grain size distribution (GSD) of a tephra sample can be described using a log-normal

66 function characterized by a median, which represents the median diameter of particles

67 comprising the grain size distribution (Md_ϕ), and a sorting value (σ_ϕ), which describes the

68 dispersion of the distribution from the Md_ϕ (Inman 1952). GSDs are often more complex than

69 implied by these two parameters, presenting multiple modes and skewed distributions. These

70 complexities arise from a broad range of processes, including size-selective sedimentation

71 processes (e.g. particle aggregation, convective instabilities; Carey and Sigurdsson 1982; Durant

72 et al 2009; Manzella et al 2015), different density distributions of pyroclasts of different origins

73 (i.e., lithics vs juvenile), and/or additional fragmentation (e.g. comminution in pyroclastic

74 density currents, PDCs) and sedimentation processes (e.g., co-PDC plumes) (Eychenne et al

75 2012; Watt et al 2015; Eychenne et al 2015). As a result, the dynamics of volcanic eruptions and

76 fragmentation processes can only be fully understood in terms of the total grain size distribution

77 (TGSD) of tephra deposits, which is typically difficult to characterize. TGSD also represents a

78 critical eruption source parameter necessary for accurate numerical simulations of eruption

79 forecasting (Mastin et al 2009; Folch 2012), and, therefore, systematic sensitivity analysis of its

80 determination and representativeness are essential (e.g., Bonadonna and Houghton 2005;

81 Volentik et al 2010; Durant et al 2012; Eychenne et al 2012; Bonadonna et al 2015; Tsunematsu

82 and Bonadonna 2015; Costa et al 2016).

83 The determination of TGSD requires a combination of detailed and widespread sampling of the

84 deposit and dedicated statistical strategies for the averaging of individual GSD analysis that can

85 deal with the non-uniform distribution of measurement sites (e.g., Voronoi tessellation

86 (Bonadonna and Houghton 2005)). TGSDs are often characterized by complex functions,

87 resulting from the combination of two or more subpopulations associated with multiple

88 fragmentation processes and/or the fragmentation of heterogeneous material (Kaminski and

89 Jaupart 1998; Volentik et al 2010; Rust and Cashman 2011; Dufek et al 2012; Bonadonna et al

90 2015; Eychenne et al 2015). Numerous theoretical and experimental studies have shown how the

91 fragmentation process can be described by fractal fragmentation theory, which approximates the

92 TGSD of the deposit using power-law functions (Turcotte 1986; Kueppers et al 2006b; Perugini

4

93 and Kueppers 2012; Costa et al 2016). In this approach, the slope of the trend (as plotted on a

94 log-log plot) represents the fractal dimension of the deposit, and the fractal dimension increases

95 with the potential energy of the fragmentation process (Perugini and Kueppers 2012).

96 In this work we provide a further characterization of the climactic phase of the 2008-2009

97 eruption of Chaitén volcano of May 6th, 2008 (Folch et al 2008; Watt et al 2009; Alfano et al

98 2011b), which largely affected populations and economic activities as far away as the coast of

99 Argentina, 600 - 800 km from the volcano. The long duration, the broad footprint of tephra

100 dispersal, the widespread impact on surrounding communities and critical infrastructures

101 (Wilson et al 2012), and the rhyolitic composition of the magma make this eruption of particular

102 interest. Prior attempts to reconstruct TGSD of the Chaitén eruption used only distal data (e.g.,

103 Watt et al 2009; Durant et al 2012; Osores et al 2013). In this work, we present a characterization

104 of GSD and componentry observed in the proximal area (up to 20 km away from the vent) and

105 combine them with the characteristics of the distal deposit presented by Watt et al. (2009). Our

106 final goal is to reconstruct a TGSD that is representative of the entire deposit originating from

107 the May 6th explosive phase of the 2008 Chaitén eruption and to provide insights into the

108 fragmentation processes during this event based on fractal analysis.

109

110 **The 2008-2013 eruption of Chaitén volcano (Chile)**

111 The eruption of Chaitén volcano on May 2008 interrupted a 400-year period of quiescence (Watt

112 et al 2011; Amigo et al 2013; Lara et al 2013). The volcano was not monitored and generally

113 considered inactive, so sparse geophysical data are available, the only exception being the

114 seismic data recorded by the regional network. These seismic data do not provide detailed

115 information about the onset of the eruption and the very first period of activity, when most

5

116 explosive phases occurred (Carn et al 2009; Lara 2009; Alfano et al 2011b). As a result, most of

117 the information about this eruption comes from remote sensing retrievals (Carn et al 2009; Watt

118 et al 2009) and field observations of the volcanic deposit and products (Castro and Dingwell

119 2009; Martin et al 2009; Watt et al 2009; Alfano et al 2011b; Alfano et al 2012; Durant et al

120 2012; Lara et al 2013; Major et al 2013; Pierson et al 2013).

121 The eruption started during the night between May 1st and May 2nd, 2008, producing a first

122 explosive phase during which about 0.5 km^3 of pyroclastic products were erupted and dispersed

123 over a wide area, reaching the Atlantic coast of Argentina (Watt et al 2009; Alfano et al 2011b;

124 Durant et al 2012). This variably explosive phase lasted for approximately 10 days, with a

125 climax on May 6th, when a sub-Plinian explosive phase produced a 18-20 km high, dark-grey

126 sustained plume (based on remote sensing; Carn et al 2009) that deposited a tephra layer of about

127 0.3 km^3 NE of the vent (Alfano et al 2011b). Geophysical observation indicate that on May 12th

128 the extrusion of a new rhyolitic dome started, ending the initial explosive phase of the eruption

129 (Lara 2009, Alfano et al 2011b). The proximal deposit consists of a complex sequence of

130 individual layers with grain size ranging from lapilli to ash, and occasional large bomb-sized

131 pumices. The upper layers are typically up to a few centimetres thick, and are often

132 discontinuous and cannot be followed throughout the entire deposit. In contrast, the tephra

133 deposit associated with the climactic event of May 6th 2008 (layer β, Alfano et al 2011b), which

134 is at the base of the stratigraphic sequence, is a massive lapilli-clast layer with thickness up to 17

135 cm (~ 5 km from the vent). Tephra samples of layer β include three main components that were

136 identified in previous studies of this eruptive event (Castro and Dingwell 2009; Alfano et al

137 2011b; Alfano et al 2012; Castro et al 2012). The most frequent component is represented by

138 grey blocky and foliated clasts, poorly vesicular, finely crystalline, and occasionally with a

139 reddish colour due to alteration. These clasts are rhyolitic and interpreted as lithic material

140 derived from disruption of the pre-existing lava dome (Alfano et al 2011b; Alfano et al 2012).

141 The second and third components, which account for smaller proportions of the deposit

142 compared to the lithic fraction, are represented by non-altered obsidian fragments and highly

143 vesicular, aphyric, sub-angular pumices (Castro and Dingwell 2009; Alfano et al 2011b; Alfano

144 et al 2012; Castro et al 2012). These two components are interpreted as juvenile products, as they

145 have similar rhyolitic composition (i.e. 74.18 and 74.11 SiO_2 wt% for pumices and obsidians,

146 respectively; Alfano et al 2011b). Field evidence indicates that these two components were

147 erupted simultaneously (Castro et al 2012).

148 The climactic explosive event of May 6thwas characterized by the rapid rise and the violent

149 fragmentation of a volatile-rich magma batch triggered by a sudden decrease of pressure (10

150 MPa s^{-1}) associated with the failure of the pre-existing obsidian dome (Alfano et al 2012). The

151 second phase of the eruption was characterized by the extrusion of an obsidian dome and

152 episodic small Vulcanian explosions with associated plumes and PDCs (Alfano et al 2011b;

153 Major et al 2013).

154 The products of the first phase of the explosive activity were mainly deposited in Argentina, to

155 the East of the volcano, between May 1st and May 13th.This phase was characterized by several

156 explosive events, producing plumes with height above 10 km. Watt et al. (2009) identified a SE

157 lobe, correlated with the activity between May 1st and May 5th, and a NE lobe correlated with

158 the activity of May 6th (Watt et al 2009; Alfano et al 2011b). However, several eruptive events

159 (May 2nd, 7th, 8th and 10th) produced fallout sedimentation in the same area as the May 6th

160 explosion (Martin et al 2009; Watt et al 2009; Osores et al 2013). After May 13th, activity

161 shifted to a less explosive style, events became less intense and produced smaller plumes (< 10

162 km high) that left no significant deposits in Argentina (Watt et al 2009).

163

164 **Methodology**

165 *Deposit characterization, componentry, grain size and particle density*

166 The proximal tephra samples of the May 6th climactic phase of the 2008-2013 Chaitén eruption

167 (Layer β; Alfano et al 2011b) were collected between 3 and 20 km from the vent in January 2009

168 (Fig. 1). Grain-size and componentry analysis were partly carried out in situ (down to 8 mm

169 diameter), and partly in the laboratory, using an optical stereoscopic microscope (on grain size

170 between 2 and 0.5 mm) and a SEM (JEOL JSM7001F) on grain size smaller than 0.5 mm at the

171 University of Geneva.

172 Grain-size analyses were conducted by dry sieving down to 0.5 mm ($\phi = 1$) for 22 samples

173 separating the products in full ϕ classes ($-\log_2$ of particle diameter in mm). The coarse fraction

174 (i.e. diameter $\geq$ 8 mm; $\leq$ -3ϕ) was sieved in situ in order to reduce the possible breakage of

175 coarse clasts, modifying the original GSD. The size fraction > 0ϕ (i.e. diameter < 0.5 mm) was

176 analysed using a laser diffraction grain-sizer (CILAS 1180; http://www.cilas.com/) down to 10ϕ

177 (i.e. 1 μm). The combination of the dry sieving analyses and laser diffraction analyses was

178 carried out as described by Eychenne et al (2012). The GSD measured through laser diffraction,

179 expressed in volume %, was converted into mass % using the density of particles in each grain

180 size class. The variation of particle density with grain size was determined using a high precision

181 water pycnometer (Fig. 2). These analyses were carried out on ash samples with particle sizes

182 between 2 mm and 250 μm, following the methodology described by Eychenne and Le Pennec

183 (2012). The lowest grain-size limit for density analysis was imposed by the scarce fraction of

184 fine ash in the samples; the density of particles smaller than 250 μm was assumed constant due

185 to their low and homogeneous vesicularity (Bonadonna and Phillips 2003; Alfano et al 2011a).

186 The resulting mass distribution was then scaled to the mass fraction of the size class analysed

187 (<0.5 mm), obtaining the final GSD of each analysed sample. Results were analysed using

188 KWare SFT 2.22.0170[1] (Wohletz et al 1989) to determine median and sorting coefficient (i.e.,

189 Md_ϕ and σ_ϕ; Inman 1952) and deconvolved to identify subpopulations and their relative

190 proportions. GSD analysis was carried out by deconvolving the distribution using log-normal

191 functions, following the procedure of Wohletz et al (1989) and optimizing the results until the

192 sum of the fractions of the subpopulation equalled 1. Results were compared with the grain size

193 parameters of the samples of the distal deposit (Watt et al 2009). Componentry was determined

194 for 11 samples located along the dispersal axis (cf., Fig. 1) to a distance of ~25 km by hand-

195 picking individual clasts down to 0.5 mm. More than 75 wt% of the whole sample was processed

196 in each case.

197

198 *Total grain size distribution*

199 TGSD was determined by applying the Voronoi tessellation method (Bonadonna and Houghton

200 2005) on the combined dataset of Alfano et al. (2011b) and Watt et al. (2009) using a dedicated

201 MATLAB code (Biass and Bonadonna 2014) and assuming that the isoline of zero mass

202 corresponded to the 0.1 mm isopach (Watt et al 2009; Alfano et al 2011b). However, the

203 combination of the two datasets does not produce uniform coverage of the fallout deposit. In

204 fact, GSD data are missing for three relatively large sectors: a medial area (Z1, 20-140 km from

205 the vent), a medial/distal area (Z2, 260-380 km from the vent), and a distal area (Z3, 570-770 km

---

[1]http://www.ees.lanl.gov/geodynamics/Wohletz/SFT.htm

206   from the vent). In order to assess the representativeness of the resulting TGSD, selected synthetic

207   GSD data were extrapolated based on observed features of proximal and distal deposits and

208   added to the total dataset before application of the Voronoi tessellation strategy, following a

209   similar approach introduced by Bonadonna et al. (2015) for the tephra deposit associated with

210   the 2011 Cordón Caulle eruption. The extrapolation was based on the estimation of Md_ϕ and σ_ϕ,

211   and the fractions of lapilli (X_l; 64 mm > d > 2 mm), coarse (X_c; 2 mm > d > 64 μm) and fine (X_f;

212   < 64 μm) ash at specific locations. First, thematic maps describing the variation of Md_ϕ, X_l, X_c

213   and X_f through the deposit were compiled; σ_ϕ is nearly constant for all samples (i.e., standard

214   deviation of the σ_ϕ values is 0.4). Therefore, we considered σ_ϕ to be constant for the entire

215   deposit and equal to 1.7ϕ (average of the σ_ϕ of all GSD). Second, the extrapolated values of Md_ϕ,

216   X_l, X_c and X_f were used to determine a synthetic GSD at the selected locations. Sensitivity

217   analyses were also carried out to estimate the number of synthetic points required to obtain stable

218   results, and to assess the relative influence of different portions of the deposit (i.e. Z1, Z2, Z3

219   and Z1+ Z2) on the TGSD determination (details on the synthetic GSD determination and

220   sensitivity analysis are described in the appendix). Finally, in order to assess the potential

221   contribution of later explosive events to the distal tephra deposit associated with the Chaitén

222   climactic phase, TGSD was also calculated reducing the mass load measured at distances >150

223   km from the vent (i.e. for all measurement sites beyond the proximal region) to 80% and 60% of

224   their original value. This is justified by examination of GSD in the distal 6th May deposit, which

225   shows clear bimodality, with a dominant coarse mode assumed to represent the 6th May deposit

226   (accounting for 50 – 80% of the deposit at individual sites) and a finer mode which may partly

227   reflect deposition of tephra from additional explosive phases (e.g. phases on May 2nd and May

10

228 8th; Fig. 3). As a result, eight distinct datasets were compiled and used to calculate the TGSD

229 (Table 1).

230

231 *Determination of particle number distribution*

232 Particle number distribution (PND) was assessed to obtain insights into the fragmentation

233 process (Turcotte 1986; Kaminski and Jaupart 1998; Kueppers et al 2006a; Kueppers et al

234 2006b; Rust and Cashman 2011; Perugini and Kueppers 2012) using the method described by

235 Kaminski and Jaupart (1998). The number of particles of a given grain size class (N_ϕ) is the ratio

236 between its mass (M_ϕ) and the mass of the average fragment representing that class (m_ϕ):

237 $$N_\phi = \frac{M_\phi}{m_\phi} = M \frac{C_\phi}{V_\phi \cdot \rho} \qquad (1)$$

238 where M is the total mass and C_ϕ is the fraction % of the ϕ grain-size class; the value of m_ϕ was

239 determined by multiplying the volume (V_ϕ) of the average fragment (assumed to be a sphere with

240 diameter equal to the mid-interval between two grain size classes) and the average fragment

241 density (ρ). PND was determined for individual samples (GSD-PND) and for the total deposit

242 (TGSD-PND).

243 GSD-PND cannot be calculated following eq. 1 because a value of total mass for an individual

244 sample is not easy to define. Therefore, GSD-PND was calculated as the number of particles

245 included in 1 m^3 of sample. The associated mass was obtained multiplying the unit volume by

246 the density of the deposit (i.e., 1250 kg/m^3 for the proximal area (Alfano et al 2011b), and 997

247 kg/m^3 for the distal area (Watt et al 2009)). As the mass of a unit volume is known, GSD-PNDs

248 can be obtained following eq. 1. The resulting GSD-PND trends were then combined using a

249 convolution approach to estimate a PND referenced to the entire deposit (Conv-PND). This

250 methodology calculates the average N_ϕ of individual samples. For lapilli clasts, with grain size

251   between 1ϕ and -6ϕ (2-64 mm), only the samples in the proximal deposit were considered; for

252   fine ash, with grain size $> 4\phi$ (< 63 μm), only the samples of the distal deposit were considered;

253   for coarse ash, with grain size between 1ϕ and 4ϕ (2 mm – 63 μm), samples of the proximal and

254   distal deposit were both considered. The resulting convolution was then multiplied by the total

255   volume of the deposit (1.8 x 10^{-1} km^3; Alfano et al, 2011b) to obtain the distribution of the total

256   number of particles and compare it with the PND derived from the Voronoi TGSD. TGSD-PND

257   was calculated considering a total mass equal to 2.3 x 10^{11} kg (obtained by multiplying the total

258   volume by the deposit density; Alfano et al 2011b) and the TGSD obtained using the Voronoi

259   method. As a result, the Conv-PND and TGSD-PND both represent the absolute number of

260   particles of a given grain-size class in the entire tephra deposit. GSD-PND, Conv-PND and

261   TGSD-PND were plotted on a log-log plot of the number of particles against the equivalent

262   particle diameter and fitted with a power-law function to determine the relative exponent

263   describing the distribution (Kaminski and Jaupart 1998; Kueppers et al 2006a; Perugini and

264   Kueppers 2012).

265

266   **Results**

267   *Characterization of the tephra deposit*

268   The componentry characteristics of the fine-ash fraction was qualitatively analysed based on

269   SEM images (Fig. 3). We found the fine fraction in the samples is mainly composed of poorly-

270   vesicular blocky grains. Due to the fine grain-size of this material, it is difficult to discriminate

271   between components in all cases, but the angular nature, low to absent vesicularity and finely

272   crystalline nature of many clasts suggests that the lithic component makes up a major proportion

273   of these samples. Vesicular clasts are also frequent, but in most cases these clasts are sparsely

274 vesicular. Highly vesicular pumice clasts are rare. Fine glass fragments, likely originating from

275 bubble wall disruption, and sometimes with star-shaped morphology, are common, and likely

276 represent glass formed in the interstices of bubbles. This latter set of clasts is interpreted as

277 representing juvenile components.

278 In the distal deposit (i.e. all measurement sites in Argentina; Fig.3), individual layers,

279 corresponding to the proximal stratigraphy, were not observable. However, deposits derived

280 from individual explosive phases can be inferred by comparing the lobate deposit distribution

281 with satellite imagery of the transport direction of individual explosive phases (Fig.3a). This

282 demonstrates that the northerly lobe of the deposit results from the 6th May explosion, with

283 possible additional contributions from the May 2nd and May 8th explosive phases. Assuming

284 that our interpretation of layer β as the proximal 6th May deposit is correct, then we can combine

285 grain-size information from the distal northern lobe with the proximal layer β, to derive a total

286 grain-size distribution for the 6th May event.

287 The nature of the distal 6th May deposit is best considered by comparison with additional lobes

288 in the distal deposit. Figure 3b compares the grain-size distributions at a distance of ~150 km

289 between the 3rd, 2nd/5th and 6th May lobes. The unimodality of the 3rd and 2nd/5th May

290 deposits, with a mode at ~4 phi, contrasts strongly with the bimodal 6th May deposit, with a

291 narrow, coarser mode at 1.5 phi. The 6th May sample has a secondary mode at ~4 phi, and it is

292 plausible that this sub-population represents deposits from the 2nd or 8th of May. In this

293 interpretation, the 6th of May event deposited the narrow coarse mode. This represents by far the

294 coarsest ash observed in the Argentinean sample set, and supports our interpretation of this

295 material being derived from the 6th May explosion, which was the most powerful stage of the

296 eruption. Building on this interpretation, we consider the grain-size distribution of samples

297   further down-wind in the northerly lobe. Again, samples can be characterised by two sub-

298   populations, and we attribute the coarsest sub-population to the 6th of May event, which

299   indicates rapid fining of this deposit in a down-wind direction (Fig. 3c). Some of the finer sub-

300   populations within this part of the tephra deposit may also originate from the 6th May plume

301   (e.g. via aggregation processes), but we cannot discard an origin from other phases of the

302   eruption (e.g., May 2nd or 8th). No direct evidence of particle aggregation was observed within

303   the deposit itself (Watt et al., 2009).

304   SEM images of ash from the different eruption lobes show similar morphologies and vesicularity

305   patterns across all parts of the distal deposit (Fig. 3d). The 6th of May deposit at site 06-16 (150

306   km from the vent) shows that the coarse mode comprises angular, dense to sparsely vesicular

307   fragments, and similar material dominates the coarse mode further downwind, at site 07-20 (215

308   km from the vent). Similar characteristics define samples in the 3rd May lobe (samples 05-07, 80

309   km from the vent, and sample 05-22, 160 km from the vent; Fig. 3d). Although sparsely to

310   moderately vesicular particles are common, highly vesicular pumice clasts are uncommon,

311   although they do occur as a minor component in all samples (Watt et al., 2009). It is harder to

312   determine the nature of the finer fractions, which have an angular morphology that in some cases

313   is consistent with bubble-driven fragmentation, but may also plausibly be produced by other

314   fragmentation processes. In general, the observations of distal ash morphologies support the

315   proximal observations of a predominance of relatively dense (i.e. non- to sparsely-vesicular)

316   clasts over the highly vesicular pumice component within the deposit.

317   The analysis of the density of the juvenile products of layer β (i.e., pumices, obsidian and density

318   of the solid fraction obtained by analysing powdered pumices) was carried out by Alfano et al

319   (2012). Here, we completed the density analysis for the fine fraction. The Dense Rock

14

320   Equivalent (DRE) density of the juvenile products is equal to 2240 ± 14 kg/m^3, very close to the

321   DRE density of the obsidian fragments (2270 ± 30 kg/m^3), whereas the density of pumice clasts

322   (determined on individual clasts with diameter > 4 cm) is 700 ± 160 kg/m^3 (Alfano et al. 2012).

323   Density of bulk samples, for particles in the size range between 2 mm and 250 μm, was found

324   almost constant. Density values vary between 1960 ± 270 kg/m^3 (for particles with diameter

325   between 250 and 360 μm) and 2280 ± 25 kg/m^3 (for particles with diameter between 1 and 2

326   mm) (Fig. 2). Although it would be expected for larger clasts to show lower density values than

327   the finer, the difference in the measurements is smaller than their uncertainty, and therefore it is

328   safe to assume that the density has a small, perhaps insignificant, variation with grain size. We

329   assume a particle density of 2140 ± 170 kg/m^3, which is the average of the density measured

330   throughout the entire grain size interval.

331

332   *Grain-size distribution and componentry*

333   GSD of individual samples of the May 6th proximal deposit is complex, mostly showing poly-

334   modality (Fig. 4). GSDs are characterized by a main sub-population with a mode between 1.0ϕ

335   and -2.7ϕ (0.5 - 6.5 mm), and a relatively small standard deviation ($1\text{-}2\phi$). This sub-population

336   accounts for> 71 wt% of the unit. The remainder can be divided into two additional sub-

337   populations: a coarse sub-population, which represents about 20 wt% of the samples that consists

338   of particles in the size range between -5.3ϕ and 0.8ϕ with a small standard deviation ($\sim1\phi$); and

339   a fine sub-population, which represents up to 8 wt% of the samples, that consists of particles in

340   the range 0.6ϕ to 6.5ϕ, with a larger standard deviation ($1\text{-}4\phi$). Samples F23 and F24 are the

341   exception, for which the fine sub-population represents 20 wt% and 28 wt% of the whole

342   sample, respectively.

343   Componentry analyses show a dominance of the lithic fraction representing 76.6 ± 3.4 % of the

344   whole sample (Fig. 4); the juvenile fraction represents 23.4 ± 3.4 %, being roughly equally

345   divided between obsidian fragments (51.8 ± 9.3 %) and pumices (48.2 ± 9.3 %). We can infer

346   that most of tephra in the proximal deposit is not vesicular (lithics and obsidian fragments being

347   88.6 ± 3.3 % in mass). The vesicular fraction, represented by pumices, is estimated to be about

348   11.4 ± 3.3 %. As a result, aforementioned sub-populations include particles of all identified

349   componentry categories, and therefore are not simply related to grain density.

350   Md_ϕ and σ_ϕ of the proximal deposit have been plotted with respect to distance from the vent and

351   compared with the values of the distal deposit from Watt et al (2009) (Fig. 5). This plot shows

352   the sampling gap in the medial area (~20-120 km from the vent; Fig 5a). Md_ϕ decreases with

353   distance from vent following a power-law trend, varying between -2.7ϕ and 1.0ϕ, in the proximal

354   area, and 1.7ϕ and 5.0ϕ, in the distal area (Fig. 5a); σ_ϕ remains roughly constant, with average

355   value of 1.7 ± 0.4 (Fig. 5b). Md_ϕ and σ_ϕ plot consistently in the field of fallout deposits (Fig. 5b).

356   The coarse subpopulation mode falls in proximity of the main population (bulk) Md_ϕ, but is

357   better sorted. The fine subpopulation shows similar grain-size characteristics of the distal ash,

358   but falls partially outside of the top-right limit of the fallout domain suggested by Walker (1971)

359   (Fig. 5b).

360

361   *Total grain-size distribution*

362   Figures 6 and 7 show the grain-size variation of the proximal and distal tephra deposit,

363   respectively, in terms of Md_ϕ and fraction of lapilli, coarse ash and fine ash. The proximal

364   deposit is coarse (i.e. $Md_\phi < 1$; Fig. 6a) and dominated by lapilli-sized clasts (up to 150 kg/m^2;

365   Fig. 6b), with a minor fraction of coarse ash (up to 50 kg/m^2; Fig. 6c) and a relatively negligible

16

366   fraction of fine ash (1-2 kg/m^2; Fig. 6e). The distal deposit is mostly composed of coarse and fine

367   ash with Md$_\phi$> 1 (d < 2 mm; Fig. 7).

368   Figure 8 describes the decay trends of the grain-size parameters over the whole deposit. Md$_\phi$

369   increases with the distance from the vent as a result of the decrease of particle grain size

370   following two exponential decay fitting trends (regression lines: Md$_\phi$ = 0.2x - 4.4, R^2 = 0.96;

371   Md$_\phi$= 0.003x + 1.2; R^2 = 0.99; Fig. 8a), with a significantly faster rate up to about 27 km from

372   the vent (i.e., break-in-slope in Fig. 8a). Lapilli fragments occur only in the proximal area, as the

373   mass load decreases rapidly with the distance from the vent, reaching zero at about 40-50 km

374   (regression line: y = 1.8 · 10^3 e$^{-0.269x}$, R^2 = 0.93; Fig. 8b). Therefore, no lapilli are expected to be

375   observed in the medial area. Coarse ash is distributed through the entire deposit, having a very

376   rapid decay in the proximal area up to about 48 km from the vent (break-in-slope in Fig. 8c), and

377   decaying very gradually in the distal area (regression lines: y = 94 e$^{-0.081x}$, R^2 = 0.99; y = 2 e^{-}

378   $^{0.004x}$, R^2 = 0.99). Finally, fine ash is dispersed mainly in the distal area and is characterized by an

379   exponential decay trend that follows the decay trend of coarse ash (regression line: y = 2.5 e^{-}

380   $^{0.004x}$, R^2 = 0.97; Fig. 8d).

381   As mentioned above, the TGSD was reconstructed both for the original dataset (dataset A) and

382   for additional datasets including various synthetic points coinciding with sampling gaps in the

383   medial deposit (datasets B to F) and various reductions of mass/area values associated with the

384   distal deposits to account for possible contribution of later explosive events (datasets G and H)

385   (Fig. 9 and appendix). The TGSD associated with datasets A (original dataset) and B (accounting

386   for data interpolation within sampling gaps) show significant differences (Fig. 9b). Dataset A

387   (Md$_\phi$ = 3.6; σ$_\phi$ = 2.5) results in a strongly bi-modal TGSD, with similar fraction of coarse (49 %)

388   and fine (41 wt%) ash, and a minor amount of lapilli (10 wt%). The bimodality becomes less

389   pronounced in the TGSD of dataset B, which is also slightly coarser ($Md_\phi = 2.6$; $\sigma_\phi = 2.5$; Fig.

390   10). In fact, the fraction of coarse ash is higher (62 wt%), while the fraction of both fine ash and

391   lapilli is lower (29 wt% and 9 wt%, respectively).

392   In order to assess the effect of the addition of synthetic points, TGSD was also calculated for

393   reduced datasets and compared with dataset B (Figs 9 and 10) in order to evaluate the weight of

394   the three zones Z1, Z2 and Z3 in the calculation. The tessellation map implemented to show the

395   absolute mass associated with individual polygons indicates that the three zones include a

396   significant portion of the mass of the deposit (up to $> 10^6$ kg) (Fig. 9a). In particular, we have

397   sequentially removed the points of Z1 (dataset C), Z2 (dataset D), Z3 (dataset E), and both points

398   of Z1 and Z2 (dataset F) from dataset B (cf., Table 1). Results indicate that the lack of

399   observations in all the areas can influence the calculations. In fact, TGSD from dataset C ($Md_\phi =$

400   2.9; $\sigma_\phi = 2.4$) results in an underestimation of coarse ash (- 4.6 wt%) and an overestimation of

401   fine ash (+ 3.4 wt%), whereas there is no significant variation for lapilli (+ 1.2 wt%). TGSD

402   from dataset D ($Md_\phi = 2.7$; $\sigma_\phi = 2.5$) results in a similar underestimation of coarse ash (-4.9

403   wt%) and larger overestimation of fine ash (+ 4.6 wt%), with almost no major variation in the

404   lapilli fraction (+ 0.3 wt%). TGSD from dataset E ($Md_\phi = 2.7$; $\sigma_\phi = 2.5$) does not result in

405   significant variation of coarse and fine ash fractions (-1.8 wt% and + 1.5 wt% respectively), nor

406   of the lapilli fraction (+ 0.8 wt%). TGSD from dataset F ($Md_\phi = 3.3$; $\sigma_\phi = 2.0$) is significantly

407   different, with large underestimation of coarse ash (- 10.3 wt%) and overestimation of fine ash (+

408   8.8 wt%) and a small overestimation of the lapilli fraction (+ 1.5 wt%).

409   The possible influence of the amalgamation of products from multiple individual explosive

410   phases (i.e. deposits from May 2nd and May 8th within the same region as the May 6th event)

411   was investigated. In order to account for possible increase of the mass load in the distal area due

18

412   to amalgamation of multiple ash layers, the values of mass/area of the distal points (beyond

413   about 150 km from vent) was reduced to 80 wt% (dataset G) and 60 wt% (dataset H). The TGSD

414   results do not show significant variation from the TGSD obtained using dataset B (Fig. 9 and

415   10), with associated Md_ϕ values of 2.5ϕ and of 2.4ϕ for both datasets, and variation in the

416   relative fractions of lapilli, coarse and fine ash < 5 wt%.

417

418   *Particle number distributions*

419   Power-law best fits of GSD-PND of distal deposits are characterized by exponents slightly

420   higher than those associated with the proximal deposit, with an average value of 2.6 ± 0.3

421   (average exponent or proximal and distal deposit is 2.4 ± 2.5 and 2.7 ± 0.2, respectively) (Fig.

422   11a). In addition, the TGSD-PND associated with dataset A and B, and Conv-PND (obtained

423   through convolution of GSD-PNDs of dataset A) are characterized by very similar power-law

424   exponents (2.9, 3.1 and 3.0 for Conv-PND and TGSD-PND of datasets A and B, respectively;

425   Fig. 11b). TGSD-PND of dataset B also shows a good correlation with the vesicle size

426   distribution (VSD; Fig. 11c).

427

428   **Discussion**

429   The long-lasting eruption of May 2008-August 2013 of Chaitén volcano produced rhyolitic

430   tephra that dispersed over an area of about $4 \cdot 10^5$ km^2; about 0.3 km^3 of material was erupted

431   during the climactic event of May 6th (i.e., total volume erupted is estimated to be about 1 km^3;

432   Watt et al 2009; Alfano et al 2011b; Bonadonna and Costa 2012).The climactic event was

433   characterized by a sub-Plinian sustained column that, according to a new estimation based on the

434 distribution of the maximum lithic fragments[2] (Carey and Sparks 1986), results in a plume height

435 of 14 km (above sampling height, a.s.h.; between sea level and 700 m a.s.l.), which is lower than

436 both the original estimation of 19 km a.s.h. of Alfano et al (2011b), and the evaluation based on

437 remote sensing (20 km above sea level) (Carn et al 2009). This lower plume height estimate is

438 likely related to the fact that the 3.2 cm isopleth contour is associated with sedimentation from

439 plume margins (e.g., Bonadonna et al 2013). In contrast, the remote sensing observation is more

440 likely associated with the peak intensity of the eruption.

441

442 *Componentry of the Chaitén* 2008 *eruption*

443 Layer β, attributed to the May 6th explosion, is composed mainly of non-vesicular fragments of

444 lithic origin (77 ± 3 wt%) associated with a minor juvenile fraction composed equally of non-

445 vesicular obsidian fragments and pumices. As a result, the products of this explosion are almost

446 entirely composed of non-vesicular dense products, i.e. lithic and obsidian clasts (~89 wt%). The

447 predominance of non-vesicular fragments explains the constant particle density across grain size

448 classes (cf. Fig. 2). The dominance of a relatively dense fraction throughout the May 6th deposit

449 is supported by examination of the distal ash deposit, which is dominated by dense and sparsely

450 vesicular clasts, inferred to correspond with the lithic fraction observed in the proximal Layer β.

451 In the proximal area, Layer β is distinctive, and defined by a much coarser grain size than

452 overlapping deposits from additional eruptive phases. The fragments within this coarse

453 population are angular and dense to sparsely vesicular, showing no significant vertical gradation.

454 These characteristics support our interpretations that relate the eruption dynamics of the May 6th

455 explosion to the disruption of the pre-existing rhyolitic dome (Alfano et al 2012), producing a

---

[2] This estimation corrects and updates the previous estimation of Alfano et al. (2011b) and is based on the isopleth map presented in the same work. In the previous version the estimate was erroneous due to an overestimation of the downwind limit of the 3.2 cm isopleth.

456 relatively short-lived eruptive column (< 2 hours; Alfano et al 2011b). It is however, interesting

457 to note that earlier phases of the distal deposit (e.g. May 3rd lobe, Fig.3d) share similar

458 characteristics to the May 6th deposit, with highly vesicular clasts being rare throughout the

459 distal ash samples, suggesting that a juvenile component may have been a relatively minor

460 constituent to much of the initial and most explosive phases of the Chaitén eruption. As

461 mentioned earlier, the new dome started growing only after May 12th (Lara 2009, Alfano et al

462 2011b), so that the non-vesicular material must belong to the previous dome.

463 Tephra deposits in the proximal area are characterized by poly-modal grain-size distributions.

464 De-convolution using SFT identified the presence of a main sub-population combined with a

465 coarser and a finer sub-population (cf., Fig. 4). The coarse sub-population is probably related to

466 fallout from plume margins. In fact, a plume of about 14-20 km above the vent is associated with

467 a corner position (transition between vertical plume and horizontal cloud) of about 5 km from

468 vent based on the theoretical relation of Bonadonna and Phillips (2003). Considering that our

469 sample locations of the proximal deposit are located between 3 and 20 km from the vent, many

470 of them (cf., Fig. 2) can be considered representative of the plume-margin fallout. This

471 corresponds to the first break-in-slope observed in the thinning decay of the tephra deposit (i.e.

472 ~4 km; Alfano et al. 2011b). The fine sub-population represents a small fraction of the bulk

473 sample (> 10 wt%), with the exception of two samples (F23 and F24) located at the northern

474 margin of the tephra deposit (> 10 km from the vent; cf. Fig. 1). The presence of a fine grained

475 sub-population could be associated both with a co-PDC component (e.g., Eychenne et al 2012)

476 and with size-selective processes, such as particle aggregation and convective instabilities (e.g.,

477 Brown et al 2010; Carazzo and Jellinek 2013; Manzella et al 2015; Durant 2015). PDCs were

478 documented but, based on the damage produced to vegetation, were considered to be

21

479 characterized by low energy and small runout distances (between 0.7 and 6 km from the vent;

480 Major et al 2013). These characteristics suggest that the co-PDC ash represents a negligible or

481 small contribution to the total tephra deposit. In contrast, the higher fraction of the fine sub-

482 population observed for the two samples in the northern margin of the fallout deposit (F23 and

483 F24) and the coarse and fine ash decay trends (cf., Fig. 6 and 7), suggest that size-selective

484 processes (e.g., aggregation) might have had a significant role in the sedimentation of the

485 products. The decay trend of fine ash mostly follows the decay trend of coarse ash, but there is

486 the caveat that the fine sub-population in this region is potentially the product of earlier or later

487 eruption phases (May 2nd and May 8th; Figure 3), making it difficult to reach unequivocal

488 conclusions. In fact, the overall thinning trends do not show significant deviations from typical

489 exponential trends which could be related to size-selective sedimentation processes (e.g. particle

490 aggregation, convective instabilities). However, size-selective sedimentation processes have

491 already been observed to occur even without strong evidence in the deposit (as when aggregates

492 are fragile they are typically not preserved in the deposit; (e.g., Bonadonna et al 2002;

493 Bonadonna et al 2011) and when the thinning trend is not significantly affected (e.g. Bonadonna

494 and Phillips, 2003).

495

496 *Reconstructing the TGSD of the whole deposit*

497 Long-lasting explosive eruptions can result in complex tephra deposits that, due to the multiple

498 explosive pulses and the wide dispersal of the products, are difficult to characterize. The May 6th

499 sub-Plinian event represents the climactic phase of the 2008-2013 Chaitén long-lasting eruption,

500 and, therefore, the reconstruction of the associated TGSD requires an accurate correlation

501 between proximal and distal deposits. In addition, the proximal and the distal deposits were

502 collected independently and present large sampling gaps (i.e., Watt et al 2009; Alfano et al

503 2011b). The deposit associated with the climactic phase could be well characterized in proximal

504 areas based on stratigraphic evidences (layer β of Alfano et al. 2011b); however the proximal

505 stratigraphy is not evident in distal area (beyond 120 km from vent), but could be identified

506 based on changing wind patterns, which produced discrete lobes of deposition (Watt et al 2009).

507 Considering that the climactic phase had the highest plumes and the largest dispersal of the

508 whole 2008-2013 eruption, with a cloud spreading NE, we assume that it was associated with the

509 coarsest subpopulation within the NE depositional lobe, as described by Watt et al. (2009) (c.f.

510 Fig3). Nonetheless, we cannot exclude the possibility that additional explosive events also

511 contributed to the sedimentation of the NE lobe, particularly in the finer sub-populations. In

512 addition, a minor portion of the products (at fine-ash grain sizes) were lost due to sedimentation

513 into the ocean. These challenges in unambiguously and fully characterising a discrete May 6th

514 distal deposit could introduce some errors in estimates of both erupted mass and TGSD for the

515 May 6th deposit.

516 Alfano et al. (2011b) carried out a sensitivity analysis on the calculation of the erupted mass,

517 showing that small uncertainties in the (mm-scale) deposit thickness over the distal region,

518 arising from the above issues, does not result in significant errors in volume estimates. Here, we

519 further investigated the effect of these issues on the determination of the TGSD. Our results

520 show that reducing the thickness of the distal May 6th deposit (beyond 150 km from vent) to

521 80% and 60% of the original value does not produce significant variation in the fraction of

522 coarse and fine ash (< 5%) in the TGSD. This is likely due to the fact that most of the mass is

523 desposited in proximal to medial areas, and, therefore, a small variation of the distal deposit

524 thickness does not significantly affect the determination of either erupted mass nor TGSD. We

525   want to stress that our results do not imply that amalgamation of products of different explosive

526   events in a tephra deposit is irrelevant, but that a critical interpretation of tephra deposits is a

527   crucial aspect of the characterization of eruptive parameters, such as erupted mass and TGSD.

528   Finally, we also explored the effect of sample distribution on the determination of TGSD. The

529   May 6th explosion was characterized by a relatively short duration (> 2 h) and produced a

530   massive deposit, without any significant vertical gradation (Alfano et al 2011b). Therefore, the

531   main parameter influencing the determination of the TGSD is the areal distribution of the sample

532   points. In particular, 22 samples and 42 samples were studied for grain-size data in proximal and

533   distal areas, respectively (cf., Fig. 1, 6 and 7). Such a sample distribution covers most of the

534   dispersal area of the Chaitén eruption climactic (May 6th) phase, with gaps between 20 and 120

535   km from vent (Z1), 260 and 380 km from vent (Z2), and 580 and 760 km from vent (Z3) (cf., Fig

536   5a and 9b). Even though the Voronoi Tessellation method is designed to deal with non-uniform

537   distributions, our results show how the lack of samples in a large part of the deposit can

538   influence the final TGSD. In fact, the Voronoi tessellation applied to the original dataset results

539   in a bimodal distribution, in which fine ash represents the largest fraction (i.e., $Md_\phi = 3.6$, $\sigma_\phi =$

540   2.5), while the Voronoi tessellation applied to the original dataset combined with 9 synthetic

541   points (dataset B) reduces the bimodality and shifts the distribution towards the coarse ash (i.e.,

542     $Md_\phi = 2.6$, $\sigma_\phi = 2.5$; cf.; Fig. 9b). In particular, the gaps associated with the sectors Z1 and Z2

543   influence greatly the TGSD calculation, as they coincide with an area of inferred high

544   accumulation of coarse ash fallout (Figs 8 and 9a). As a result, the presence of these two

545   sampling gaps creates a shift of the TGSD towards the fine ash (i.e., $Md_\phi = 3.2$, $\sigma_\phi = 2.0$; cf., +

546   14.4 wt%; cf., Fig. 10), and underestimates the coarse ash fraction (- 16.2 wt%). The Voronoi

547   strategy cannot capture this shift in fallout regime and results in a bimodal distribution, which is

24

548 very likely not related to the eruption dynamics but to an artefact of the sample distribution. A

549 similar approach was also applied for the characterization of the TGSD associated with the 2011

550 Cordón Caulle eruption, for which most distal data were missing (Bonadonna et al 2015).

551 However, the TGSD of the Cordón Caulle eruption associated with the addition of distal

552 synthetic data did not result in significant difference from the original dataset. These results

553 mirror the results obtained calculating the TGSD using dataset E. The GSD that can be observed

554 at the margins of the distal region is probably nearly constant, and therefore fewer datapoints can

555 be enough for a reliable TGSD computation. On the other hand, in the medial/distal region,

556 where the GSD can present greater variations, the presence of sampling gaps can be critical and

557 compromise the calculation of the TGSD. Based on these results, we suspect that the previously

558 published TGSDs (i.e., $5\phi > $ Md$\phi > 3\phi$; Watt et al 2009; Osores et al 2013) result in the

559 underestimation of the coarse ash fraction as a result of the use of an incomplete dataset, lack of

560 proximal data and with sampling gaps, and the possible inclusion, however not in large

561 proportion, of fine ash originated from other eruptive events (i.e., May 2nd and May 8th; cf., Fig.

562 3).

563

564 *Insights into fragmentation process from grain size observations*

565 TGSD results (i.e. dataset B in Fig. 9b) show that the May 6th 2008 Chaitén explosion was

566 characterized by the generation of a large amount of ash (d < 2 mm), representing 98 wt% of the

567 products, mainly falling in the size range of the coarse ash (2 mm > d >63 μm; 77 wt%). The

568 associated TGSD-PND is characterized by a power-law exponent (3.0), falling in the lower end

569 of the range typically described for fallout deposits (i.e., 3.0-3.7; Kaminski and Jaupart 1998).

570 The PND trends are concave downwards (cf., Fig. 11), which is typically observed in many PND

571   (Kaminski and Jaupart 1998; Rust and Cashman 2011; Costa et al 2016). The significance of this

572   trend has been related to the possible underestimation of values at the extremes of the

573   distribution. However, the goodness of fitting ($R^2 = 0.99$) indicates that the concavity observed

574   in our result is statistically not significant. In fact, the Log-Log plot used to study these

575   distributions smoothes possible complexities that are evident in the GSD plots (cf., Fig. 3d and

576   4). As a result, PND is not a suitable tool to characterize the complexity of the fragmentation

577   process as a whole (e.g. bimodality), yet is a very effective tool to compare different eruptions

578   and to characterize the energy involved in the explosive process based on power-law functions

579   (Kueppers et al 2006a; Kueppers et al 2006b; Perugini and Kueppers 2012).

580   TGSD-PND also follows the VSD trend (cf., Fig. 11c), suggesting a relationship between grain

581   size and vesicularity (Rust and Cashman 2011). However, most of the products are the result of

582   the fragmentation of non-vesicular material (89%), mainly from the pre-existing wall and dome

583   rocks. The textural analyses carried out on pumice samples describes the vesicularity of the

584   juvenile products as characterized by a unimodal distribution with mode falling between 0.05

585   and 0.13 mm (Alfano et al 2012). TGSD is characterized by Md_ϕ values equal to 0.16 mm (cf.,

586   2.6ϕ), which is slightly coarser than the modal range identified for the vesicles. Generally, a

587   bubble-driven ash-generation process produces clasts that are roughly of the same range of

588   dimensions as the vesicles (Rust and Cashman 2011; Genareau et al 2012; Genareau et al 2013).

589   This consideration suggests that vesicularity had only a secondary role in magma fragmentation,

590   limited to the minor vesicular juvenile fraction, and might have been responsible for the

591   production of most of the fine-ash fraction.

592   However, if vesiculation is not the main factor driving the energy of the sub-Plinian May 6th

593   event, this raises the question of what drove the violent and efficient fragmentation in the May

594 6th explosion, given the large proportion of ash generated in the event. Previous studies on

595 rhyolitic eruptions (e.g., Chaitén and Cordón Caulle) have demonstrated that despite the high

596 silica content, rhyolitic magmas can have lower viscosity than expected. In fact, a rhyolitic

597 magma stored in a shallow magmatic chamber can maintain near-liquidus hydrous conditions

598 (Castro and Dingwell 2009; Castro et al 2013; Jay et al 2014), and the viscosity can be low

599 enough to allow for a fast ascent through the crust (Wicks et al 2011). The Chaitén eruption was

600 characterized by an apparently very rapid onset, favoured by the low viscosity of the rhyolitic

601 magma, that could rise rapidly and drive fracturing of the confining wall rock/pre-existing lava

602 dome (Castro and Dingwell 2009; Wicks et al 2011). In these conditions, magma was likely

603 characterized by a high shear rate that, associated with a high decompression rate (~ 10 MPa/s;

604 Alfano et al 2012), and this could have acted as the main factor driving the violent fragmentation

605 of the magma and the pre-existing dome. The dominance of coarse ash in the TGSD and the

606 relatively low exponent of the PND trend suggest that fragmentation was relatively less efficient

607 than other explosive eruptions that may perhaps be more dominantly driven by vesiculation. Yet,

608 the production of a 15-20 km sub-Plinian column suggests that high shear and decompression

609 rate may still produce sufficient energy and ash content to produce a highly explosive, buoyant

610 eruption column, even if that material involved is dominated by non-juvenile material. Based on

611 our result and on previous work, we suggest that a better understanding of the link between

612 fragmentation dynamics, ash production, explosive energy, proportion of juvenile products and

613 the associated TGSD is required.

614

615 **Conclusions**

27

616   Based on our detailed grain-size characterization of the tephra deposit associated with the May

617   6th 2008 Chaitén eruption, we can conclude that:

618   1)   Regardless of the similarities between TGSD and PND with pumice vesicularity, the

619   erupted products of the climactic phase of the Chaitén eruption were probably the result of

620   a shear-driven fragmentation that mostly acted on the material of the old obsidian dome. In

621   fact, a bubble-driven fragmentation process is not compatible with the high proportion of

622   lithic material (76%) in the proximal deposit.

623   2)   The proximal tephra deposit (3-20 km from vent) consists of both uni- and poly-modal,

624   mostly well-sorted GSDs with Md_ϕ and σ_ϕ varying between -2.6–1.2ϕ and 0.9-3,

625   respectively. De-convolution of the GSD identified a main subpopulation dominated by

626   coarse ash and lapilli (> 71 wt% of the samples) with modes between 0.8ϕ and -2.7ϕ (0.5 -

627   8.0 mm) (probably associated with the fallout from the umbrella cloud), a smaller lapilli-

628   rich subpopulation (<20 wt%) with modes between -5.3ϕ and 0.8ϕ (probably related to the

629   sedimentation from plume margins), and a fine ash-rich subpopulation (up to 28 wt%) with

630   modes between 0.6ϕ and 6.5ϕ, (probably mostly related to size-selective sedimentation

631   processes such as aggregation or convective instabilities).

632   3)   The proximal deposit is composed mainly of lithic fragments (76.6 ± 3.4 wt%) and a

633   smaller fraction of juvenile fragments (23.4 ± 3.4 wt%); the juvenile fraction comprises

634   highly vesicular aphyric pumice and non-vesicular obsidian fragments in almost equal

635   proportions; the lithic fraction is composed of laminated grey rhyolitic fragments

636   originated by the disruption of the old dome. This conclusion is supported by the

637   dominance of dense to sparsely vesicular fragments that comprise the coarsest (May 6th)

638   fraction of the distal deposit. Highly vesicular pumice is rare in this deposit, but notably it

28

639   is also rare in other lobes of the distal deposit, formed from earlier phases of the Chaitén

640   eruption, which are also dominated by relatively dense clasts. Our results suggest

641   consistency in the componentry of the ash fraction between proximal and distal samples.

642 4) The decay trends of both Md_ϕ and coarse ash can be described by two exponential

643   segments on semi-log plots, with break-in-slope located at 16 and 31 km from the vent,

644   respectively, possibly reflecting relevant shifts in the sedimentation regime in this area. In

645   contrast, both the decay trend of lapilli and fine-ash fragments were described by only one

646   exponential segment, with the lapilli fragments going rapidly to zero within about 50 km

647   from the vent. The distal decay trend of coarse and that of fine ash are similar. Although

648   this may be associated with size-selective sedimentation processes (e.g. ash aggregation,

649   convective instabilities), it is difficult to distinguish these processes from a potential

650   overlap of the 6th May deposit with ash from additional phases (e.g. May 2nd and May

651   8th) of the Chaitén eruption.

652 5) An accurate determination of TGSD requires a wide distribution of field observations that

653   can describe the variation of grain size with distance from the vent across all critical shifts

654   in fallout regimes (e.g. from lapilli to coarse ash, from coarse to fine ash). As in the case of

655   the Chaitén eruption, when these critical parts of the deposit are not sampled (in particular

656   when they are associated with a large mass fraction of the deposit), the addition of

657   synthetic data located in critical areas appears to improve the TGSD estimate.

658 6) Our best estimate of TGSD for the climactic phase of the Chaitén 2008-20013 eruption

659   based on the addition of critical synthetic points is uni-modal and characterized by $Md_\phi =$

660   2.6 and $\sigma_\phi = 2.5$ (dataset B). When synthetic data are not considered (dataset A), TGSD

661   shows a pronounced bi-modality and a smaller fraction of coarse ash ($Md_\phi = 3.6$ and $\sigma_\phi =$

662   2.2). In particular, the area from 50 km to 350 km from the vent (zones Z1 and Z2) proved

663   critical in the case of TGSD determination for the climactic phase of the Chaitén 2008-

664   2013 eruption. Sensitivity tests also indicate that the stability of results can be reached with

665   a small number of added synthetic data (i.e., 3-5 points per each zone, 1 every 20-45 km,

666   for the case of the Chaitén eruption).

667 7) Due to the majority of products being sedimented in proximal area, the estimation of both

668   erupted mass and TGSD of the climactic phase of this long-lasting eruption is not strongly

669   affected by the possible contribution of smaller explosive events to the distal cumulative

670   tephra deposit, which are often difficult to correlate stratigraphically. The variation of

671   TGSD associated with a reduction of the thickness of the distal deposit (beyond 150 km

672   from vent) to 80% and 60% of the original value result in a relatively small variation in the

673   fraction of coarse and fine ash (< 5 wt%). Alfano et al. (2011b) had already shown that a

674   reduction of the distal thickness only resulted in the reduction of < 5 wt% of erupted mass.

675

681

682

Appendix A. Determination of synthetic points and sensitivity analysis

Three large gaps in the data sampling were identified within the tephra deposit of the May 6th 2008 Chaitén eruption (Z1: 20-140 km from the vent; Z2: 260-380 km from the vent; Z3: 570-770 km from the vent; Fig. 9a of main text). Synthetic points were estimated in order to cover the lack of data in these three areas. The points were chosen along the dispersal axis and equally spaced. In order to assess the number of synthetic points required to obtain a stable TGSD, the calculation was carried out considering 3 points (Dataset B_1; 1 point per zone), 9 points (Dataset B_2; 3 points per zone) and 15 points (Dataset B_3; 5 points per zone), respectively (Table A1). Dataset B_1 includes the synthetic points located in the middle of the zones (i.e, 80, 320 and 670 km from the vent for the areas Z1, Z2 and Z3, respectively). Dataset B_2 includes the points located at 50, 80 and 110 km from the vent for Z1; 290, 320 and 650 km from the vent for Z2; 625, 670 and 715 km from the vent for Z3. Dataset B_3 includes the points located at 40, 60, 80, 100 and 120 km from the vent for Z1; 280, 300, 320, 340 and 360 km from the vent for Z2; 610, 640, 670, 700 and 730 km from the vent for Z3 (Table A1). The Md_ϕ and the mass load of lapilli (X_l), coarse ash (X_c) and fine ash (X_f) for each of these points were estimated based on the dispersal maps of Figs 6 and 7, and using the decay-trend plots of Fig. 8 of the main text. According to the observed decay trends, no lapilli particles sedimented in these areas (Fig. 8b). Based on the extrapolated grain size parameters, a synthetic GSD for each point was determined. A normal distribution was calculated based on the Md_ϕ value for each point and using a sorting determined as the average of the values observed through the deposit (i.e. 0.4). The GSDs were then corrected for the extrapolated fraction of coarse and fine ash. The resulting GSD are shown in Fig. A1.

31

705   The GSD of the synthetic points were then used to extend the original dataset (Dataset A in Fig.

706   9b). Results of the TGSD associated with these 3 datasets are shown in Fig. A2. The difference

707   of TGSD obtained using datasets B_2 and B_3 is small, whereas dataset B_1 gives a TGSD skewed

708   toward the coarse size fraction. We conclude that three points per zone are representative for the

709   data gap of the climactic phase of the 2008-2013 Chaitén eruption and are sufficient to generate

710   stable TGSD results.

711

712 **References**

713 Alfano F, Bonadonna C, Delmelle P, Costantini L (2011a) Insights on tephra settling velocity

714 from morphological observations. J Volcanol Geotherm Res 208:86–98. doi:

715 10.1016/j.jvolgeores.2011.09.013.

716 Alfano F, Bonadonna C, Gurioli L (2012) Insights into eruption dynamics from textural analysis:

717 The case of the May, 2008, Chaitén eruption. Bull Volcanol 74:2095–2108. doi:

718 10.1007/s00445-012-0648-3

719 Alfano F, Bonadonna C, Volentik ACM, et al (2011b) Tephra stratigraphy and eruptive volume

720 of the May, 2008, Chaitén eruption, Chile. Bull Volcanol 73:613–630. doi: 10.1007/s00445-

721 010-0428-x

722 Amigo Á, Lara LE, Smith VC (2013) Holocene record of large explosive eruptions from Chaitén

723 and Michinmahuida Volcanoes , Chile. Andean Geol 40:227–248. doi:

724 10.5027/andgeoV40n2-a

725 Biass S, Bonadonna C (2014) TOTGS: Total grainsize distribution of tephra fallout.

726 https://vhub.org/resources/3297.

727 Bonadonna C, Cioni R, Pistolesi M, Elissondo M, Baumann V (2015) Sedimentation of long-

728 lasting wind-affected volcanic plumes: the example of the 2011 rhyolitic Cordón Caulle

729 eruption, Chile. Bull Volcanol 77:1–19. doi: 10.1007/s00445-015-0900-8

730 Bonadonna C, Cioni R, Pistolesi M, Connor C, Scollo S, Pioli L, Rosi M (2013) Determination

731 of the largest clast sizes of tephra deposits for the characterization of explosive eruptions: a

732 study of the IAVCEI commission on tephra hazard modelling. Bull Volcanol 75:1–15. doi:

733 10.1007/s00445-012-0680-3

734   Bonadonna C, Connor CB, Houghton BF, Connor L , Byrne M, Laing A, Hincks TK (2005)

735   Probabilistic modeling of tephra dispersal: Hazard assessment of a multiphase rhyolitic

736   eruption at Tarawera, New Zealand. J Geophys Res B Solid Earth 110:1–21. doi:

737   10.1029/2003JB002896

738   Bonadonna C, Costa A (2012) Estimating the volume of tephra deposits: A new simple strategy.

739   Geology 40:415–418. doi: 10.1130/G32769.1

740   Bonadonna C, Genco R, Gouhier M, Pistolesi M, Cioni R, Alfano F, Hoskuldsson A, Ripepe M

741   (2011) Tephra sedimentation during the 2010 Eyjafjallajkull eruption (Iceland) from

742   deposit, radar, and satellite observations. J. Geophys. Res. Solid Earth 116: B12202,

743   doi:10.1029/2011JB008462.

744   Bonadonna C, Houghton BF (2005) Total grain-size distribution and volume of tephra-fall

745   deposits. Bull Volcanol 67:441–456. doi: 10.1007/s00445-004-0386-2

746   Bonadonna C, Macedonio G, Sparks RSJ (2002) Numerical modelling of tephra fallout

747   associated with dome collapses and Vulcanian explosions: application to hazard assessment

748   on Montserrat. Geol Soc London, Mem 21:517–537. doi:

749   10.1144/GSL.MEM.2002.021.01.23

750   Bonadonna C, Phillips JC (2003) Sedimentation from strong volcanic plumes. J Geophys Res

751   Solid Earth 108:2340. doi: 10.1029/2002JB002034

752   Brown RJ, Branney MJ, Maher C, Dávila-Harris P (2010) Origin of accretionary lapilli within

753   ground-hugging density currents: Evidence from pyroclastic couplets on Tenerife. Geol Soc

754   Am Bull 122 :305–320, doi:10.1130/B26449.1

755   Carazzo G, Jellinek AM (2013) Particle sedimentation and diffusive convection in volcanic ash-

756   clouds. J Geophys Res Solid Earth 118:1420–1437. doi: 10.1002/jgrb.50155

757   Carey S, Sparks RSJ (1986) Quantitative models of the fallout and dispersal of tephra from

758   volcanic eruption columns. Bull Volcanol 48:109–125. doi: 10.1007/BF01046546

759   Carey SN, Sigurdsson H (1982) Influence of particle aggregation on deposition of distal tephra

760   from the May 18, 1980, eruption of Mount St. Helens volcano. J Geophys Res 87:7061. doi:

761   10.1029/JB087iB08p07061

762   Carn S a., Paluster JS, Lara L, Ewert JW, Watt S, Prata AJ, Thomas RJ, Villarosa G (2009) The

763   Unexpected Awakening of Chaitén Volcano, Chile. Eos (Washington DC) 90:205–206. doi:

764   10.1029/2009EO240001

765   Cas RAF, Wright JV. (1988) Volcanic Successions Modern and Ancient. doi: 10.1007/978-94-

766   009-3167-1

767   Cashman K V, Mangan MT (1994) Physical aspects of magmatic degassing; II, Constraints on

768   vesiculation processes from textural studies of eruptive products. Rev Mineral

769   Geochemistry 30 :447–478.

770   Castro JM, Cordonnier B, Tuffen H, Mark J. Tobinf MJ, Puskarf L, Marting MC, Bechtelg HA

771   (2012) The role of melt-fracture degassing in defusing explosive rhyolite eruptions at

772   volcán Chaitén. Earth Planet Sci Lett 333-334:63–69. doi: 10.1016/j.epsl.2012.04.024

773   Castro JM, Dingwell DB (2009) Rapid ascent of rhyolitic magma at Chaitén volcano, Chile.

774   Nature 461:780–783. doi: 10.1038/nature08458

775   Castro JM, Schipper CI, Mueller SP, Militzer AS, Amigo A, Parejas CS, Jacob D (2013) Storage

776   and eruption of near-liquidus rhyolite magma at Cordón Caulle, Chile. Bull Volcanol 75:1–

777   17. doi: 10.1007/s00445-013-0702-9

778   Costa A, Pioli L, Bonadonna C (2016) Assessing tephra total grain-size distribution: Insights

779   from field data analysis. Earth Planet Sci Lett 443:90–107. doi:

780   http://dx.doi.org/10.1016/j.epsl.2016.02.040

781   Costantini L, Houghton BF, Bonadonna C (2010) Constraints on eruption dynamics of basaltic

782   explosive activity derived from chemical and microtextural study: The example of the

783   Fontana Lapilli Plinian eruption, Nicaragua. J Volcanol Geotherm Res 189:207–224. doi:

784   10.1016/j.jvolgeores.2009.11.008

785   Dufek J, Manga M, Patel A (2012) Granular disruption during explosive volcanic eruptions. Nat

786   Geosci 5:561–564. doi: 10.1038/ngeo1524

787   Durant AJ, Rose WI, Sarna-Wojcicki AM, Carey S, Volentik ACM (2009) Hydrometeor-

788   enhanced tephra sedimentation: Constraints from the 18 May 1980 eruption of Mount St.

789   Helens. J Geophys Res 114:1–21. doi: 10.1029/2008JB005756

790   Durant AJ (2015) Research focus: Toward a realistic formulation of fine-ash lifetime in volcanic

791   clouds. Geol 43 :271–272. doi: 10.1130/focus032015.1

792   Durant AJ, Villarosa G, Rose WI, Delmelle P, Prata AJ, Viramonte JG (2012) Long-range

793   volcanic ash transport and fallout during the 2008 eruption of Chaitén volcano, Chile. Phys

794   Chem Earth 45-46:50–64. doi: 10.1016/j.pce.2011.09.004

795   Eychenne J, Cashman K, Rust A, Durant A (2015) Impact of the lateral blast on the spatial

796   pattern and grain size characteristics of the 18 May 1980 Mount St. Helens fallout deposit. J

797   Geophys Res Solid Earth 120:6018–6038. doi: 10.1002/2015JB012116

798   Eychenne J, Le Pennec JL (2012) Sigmoidal particle density distribution in a subplinian scoria

799   fall deposit. Bull Volcanol 74:2243–2249. doi: 10.1007/s00445-012-0671-4

800   Eychenne J, Le Pennec JL, Troncoso L, et al (2012) Causes and consequences of bimodal grain-

801   size distribution of tephra fall deposited during the August 2006 Tungurahua eruption

802   (Ecuador). Bull Volcanol 74:187–205. doi: 10.1007/s00445-011-0517-5

803   Folch A (2012) A review of tephra transport and dispersal models: Evolution, current status, and

804   future perspectives. J Volcanol Geotherm Res 235-236:96–115. doi:

805   10.1016/j.jvolgeores.2012.05.020

806   Folch A, Jorba O, Viramonte J (2008) Volcanic ash forecast – application to the May 2008

807   Chaitén eruption. Nat Hazards Earth Syst Sci 8:927–940. doi: 10.5194/nhess-8-927-2008

808   Genareau K, Mulukutla GK, Proussevitch A, Durant AJ, Rose WI, Sahagian DL (2013) The size

809   range of bubbles that produce ash during explosive volcanic eruptions. J Appl Volcanol 2:4.

810   doi: 10.1186/2191-5040-2-4

811   Genareau K, Proussevitch A, Durant AJ, Mulukutla GK, Sahagian DL (2012) Sizing up the

812   bubbles that produce very fine ash during explosive volcanic eruptions. Geophys Res Lett

813   39:1–6. doi: 10.1029/2012GL052471

814   Houghton BF, Wilson CJN (1989) A vesicularity index for pyroclastic deposits. Bull Volcanol

815   51:451–462. doi: 10.1007/BF01078811

816   Inman D (1952) Measures for describing the size distribution of sediments. J Sediment Petrol

817   125–145. doi: 10.1306/D42694DB-2B26-11D7-8648000102C1865D

818   Jay J, Costa F, Pritchard M, Lara L, Singer B, Herrin J (2014) Locating magma reservoirs using

819   InSAR and petrology before and during the 2011–2012 Cordón Caulle silicic eruption.

820   Earth Planet Sci Lett 395:254–266. doi: http://dx.doi.org/10.1016/j.epsl.2014.03.046

821 Kaminski E, Jaupart C (1998) The size distribution of pyroclasts and the fragmentation sequence

822   in explosive volcanic eruptions. J Geophys Res 103:29759. doi: 10.1029/98JB02795

823 Kueppers U, Perugini D, Dingwell DB (2006a) "Explosive energy" during volcanic eruptions

824   from fractal analysis of pyroclasts. Earth Planet Sci Lett 248:800–807. doi:

825   10.1016/j.epsl.2006.06.033

826 Kueppers U, Scheu B, Spieler O, Dingwell DB (2006b) Fragmentation efficiency of explosive

827   volcanic eruptions: A study of experimentally generated pyroclasts. J Volcanol Geotherm

828   Res 153:125–135. doi: 10.1016/j.jvolgeores.2005.08.006

829 Lara LE (2009) La erupcion 2008 del volcan Chaiten, Chile: informe preliminar. Andean Geol

830   36:125–129. doi: 10.5027/556

831 Lara LE, Moreno R, Amigo Á, Hoblitt RP, Pierson TC (2013) Late Holocene history of Chaitén

832   Volcano: New evidence for a 17th century eruption. Andean Geol 40:249–261. doi:

833   10.5027/andgeoV40n2-a04

834 Major JJ, Pierson TC, Hoblitt RP, Moreno H (2013) Pyroclastic density currents associated with

835   the 2008-2009 eruption of Chaitén Volcano (Chile): Forest disturbances, deposits, and

836   dynamics. Andean Geol 40:324–358. doi: 10.5027/andgeoV40n2-a09

837 Manzella I, Bonadonna C, Phillips JC, Monnard H (2015) The role of gravitational instabilities

838   in deposition of volcanic ash. Geol . doi: 10.1130/G36252.1

839 Martin RS, Watt SFL, Pyle DM, Mather TA, Matthews NE, Georg RB, Day JA, Fairhead T, Witt

840   MLI, Quayle BM (2009) Environmental effects of ashfall in Argentina from the 2008

841   Chaitén volcanic eruption. J Volcanol Geotherm Res 184:462–472. doi:

842   10.1016/j.jvolgeores.2009.04.010

843 Mastin LG, Guffanti M, Servranckx R, Webley P, Barsotti S, Dean K, Durant AJ, Ewert JW,

844   Neri A, Rose WI., Schneider D, Siebert L, Stunder B, Swanson G, Tupper A , Volentik

845   ACM, Waythomas CF (2009) A multidisciplinary effort to assign realistic source

846   parameters to models of volcanic ash-cloud transport and dispersion during eruptions. J

847   Volcanol Geotherm Res 186:10–21. doi: http://dx.doi.org/10.1016/j.jvolgeores.2009.01.008

848 Osores MS, Folch A, Collini E, Villarosa G, Durant AJ, Pujol G, Viramonte GJ (2013)

849   Validation of the FALL3D model for the 2008 Chaitén eruption using field and satellite

850   data. Andean Geol 40:262–276. doi: 10.5027/andgeoV40n2-a05

851 Perugini D, Kueppers U (2012) Fractal analysis of experimentally generated pyroclasts: A tool

852   for volcanic hazard assessment. Acta Geophys 60:682–698. doi: 10.2478/s11600-012-0019-

853   7

854 Pierson TC, Major JJ, Amigo Á, Moreno H (2013) Acute sedimentation response to rainfall

855   following the explosive phase of the 2008-2009 eruption of Chaitén volcano, Chile. Bull

856   Volcanol 75:1–17. doi: 10.1007/s00445-013-0723-4

857 Pyle DM (1989) The thickness, volume and grainsize of tephra fall deposits. Bull Volcanol 51:1–

858   15, doi: 10.1007/BF01086757

859 Rust AC, Cashman KV. (2011) Permeability controls on expansion and size distributions of

860   pyroclasts. J Geophys Res Solid Earth 116:1–17. doi: 10.1029/2011JB008494

861 Tsunematsu K, Bonadonna C (2015) Grain-size features of two large eruptions from Cotopaxi

862   volcano (Ecuador) and implications for the calculation of the total grain-size distribution.

863   Bull Volcanol 77:1–12. doi: 10.1007/s00445-015-0949-4

864   Turcotte DL (1986) Fractals and fragmentation. J Geophys Res Solid Earth 91:1921–1926. doi:

865   10.1029/JB091iB02p01921

866   Volentik ACM, Bonadonna C, Connor CB, Connor L, Rosi M (2010) Modeling tephra dispersal

867   in absence of wind: Insights from the climactic phase of the 2450BP Plinian eruption of

868   Pululagua volcano (Ecuador). J Volcanol Geotherm Res 193:117–136. doi:

869   10.1016/j.jvolgeores.2010.03.011

870   Walker GPL (1971) Grain-Size Characteristics of Pyroclastic Deposits. J Geol 79:696–714. doi:

871   10.2307/30065501

872   Watt SFL, Gilbert JS, Folch A, Phillips JC, Cai XM (2015) An example of enhanced tephra

873   deposition driven by topographically induced atmospheric turbulence. Bull Volcanol 77:1–

874   14. doi: 10.1007/s00445-015-0927-x

875   Watt SFL, Pyle DM, Mather T, Martin RS, Matthews NE (2009) Fallout and distribution of

876   volcanic ash over Argentina following the May 2008 explosive eruption of Chaitén, Chile. J

877   Geophys Res Solid Earth 114:1–11. doi: 10.1029/2008JB006219

878   Watt SFL, Pyle DM, Naranjo J, Rosqvist G, Mella M, Mather TA, Moreno H (2011) Holocene

879   tephrochronology of the Hualaihue region (Andean southern volcanic zone, ~42° S),

880   southern Chile. Quat Int 246:324–343. doi: 10.1016/j.quaint.2011.05.029

881   Wicks C, de la Llera JC, Lara LE, Lowenstern J (2011) The role of dyking and fault control in

882   the rapid onset of eruption at Chaitén volcano, Chile. Nature 478:374–377. doi:

883   10.1038/nature10541

884   Wilson TM, Stewart C, Sword-Daniels V, Leonard GS, Johnston DM, Cole JW, Wardman J,

885   Wilson G, Barnard ST (2012) Volcanic ash impacts on critical infrastructure. Phys Chem

886   Earth, Parts A/B/C 45–46:5–23. doi: http://dx.doi.org/10.1016/j.pce.2011.06.006

887   Wohletz K, Sheridan M, Brown W (1989) Particle size distribution and the sequential

888   fragmentation/transport theory applied to volcanic ash. J Geophys Res 94:15–703, doi:

889   10.1029/JB094iB11p15703

890

891

Figure captions

893 **Figure 1**. a) Location of Chaitén volcano. b) isopach maps (in cm) of the May 6th 2008 deposit

894 (β layer) in the proximal area (modified after Alfano et al 2011b), indicating the location of the

895 samples analysed in this work (red points indicate samples that were also processed for

896 componentry analysis. c) Isopach map (in cm) of the May 6th 2008 deposit (β layer) in the distal

897 area (modified after Alfano et al (2011b)) and indicating the location of the sample points (black

898 diamonds; Watt et al (2009)); isopach contours are obtained extrapolating the thickness values

899 from the total deposit map of Alfano et al (2011b) and accounting for possible overlap of

900 multiple depositional phases; black dashed line encloses the depositional area of the explosive

901 activity of May 3rd-5th.

902 **Figure 2**. Density distribution plot showing the values obtained through high precision water

903 pycnometer analysis. Black diamonds indicate the average value of the measurements, error bars

904 indicate the standard deviation; the grey line indicate the bulk density of the lithic samples; the

905 reddish area indicate the values of density measured for the pumice clasts (Alfano et al 2011b);

906 the black dashed line indicate a hypothetical sigmoidal distribution (Eychenne and Le Pennec

907 2012) that would be expected for a sample composed of juvenile vesicular clasts that would

908 show a trend with density increasing as the grain size decreases.

909 **Figure 3**. a) Map showing selected distal sites of the Chaitén 2008-2013 deposit, and their

910 relationship with the major explosive phases and plume transport directions (gray arrows) during

911 the eruption. The May 6th phase is affected by overlap with deposit from May 2nd and May 8th.

912 b) Grain-size distributions of selected sites ~150 km from source, showing the notably coarser

913 population attributed to the May 6th plume. c) Down-wind patterns in grain-size distributions in

914 the May 6th deposit. The coarse population (shaded areas) is attributed to May 6th, while the

915 finer mode potentially includes some component of additional eruption phases (May 2nd, 8th). d)

916 SEM images of ash samples from the distal Chaitén deposit.

917 **Figure 4**.Grain-size distribution and componentry histograms. Md_ϕ and σ_ϕ of bulk samples are

918 indicated; the red curves, where present, indicate the subpopulation identified through SFT

919 analysis; plots not showing red curves refer to samples whose SFT deconvolution resulted in a

920 single population.

921 **Figure 5**. a) Plot of Md_ϕ versus distance from the vent for bulk samples of the proximal and

922 distal sites referred to the May 6th deposit. b) Plot of Md_ϕ versus σ_ϕ where the dashed line

923 indicates the fallout field (modified after Walker (1971)); the plot includes values for the bulk

924 samples of proximal and distal sites, and the mode and dispersion values of coarse and fine

925 subpopulations identified in the proximal samples from deconvolution analysis.

926 **Figure 6**. Isoline maps of Md_ϕ (a), and mass load (kg/m^2) of lapilli (b), coarse ash (c) and fine

927 ash (d) in the proximal area.

928 **Figure 7**.Isoline maps of Md_ϕ (a), and mass load (kg/m^2) of coarse ash (b), and fine ash (c) in the

929 distal area.

930 **Figure 8**. Decay trend vs. the distance from the vent along the dispersal axis of Md_ϕ of bulk

931 samples (a), and mass load of lapilli (b), coarse ash (c) and fine ash (d) fractions. Shaded areas

932 indicate the sampling gap zones Z1, Z2 and Z3 (cf. Fig. 9). The plot for Lapilli clasts (b) includes

933 a zoomed plot to better show the trend in the proximal area.

934 **Figure 9**. Total grain size distribution. a) Voronoi tessellation associated with the combination of

935 the original dataset and the additional 9 synthetic points (i.e. polygons with red outline) (dataset

936 B). Colours show the absolute mass associated with individual polygons (i.e. mass/area of

937 samples multiplied by polygon area); c) TGSD results associated with the individual datasets.

938 **Figure 10.** Comparison of the TGSD associated with the dataset B with TGSD associated with

939 the original dataset A, datasets C, D, E and F (obtained selectively removing the synthetic points

940 of Z1, Z2, Z3, Z1+Z2,respectively), and datasets G and H (obtained reducing the mass load

941 values of the distal points, beyond 150 km from the vent, to 80 % and 60 %, respectively).

942 **Figure 11**. a) Variation of the GSD-PND power-law exponents with distance from the vent; b)

943 Cumulative Log-Log plots of TGSD-PND, obtained from the Voronoi tessellation using datasets

944 A (regression line: $y = 2.7 \cdot 10^5 x^{-3.1}$, $R^2 = 0.98$) and B (regression line: $y = 3 \cdot 10^5 x^{-3.0}$, $R^2 = 0.98$)

945 (Fig. 8c), and Conv-PND (regression line: $y = 4.5 \cdot 10^5 x^{-2.9}$, $R^2 = 0.99$), obtained by convoluting

946 the GSD-PND trends; c) Cumulative Log-Log plot comparing TGSD-PND associated with

947 dataset B together with the VSD (regression line: $y = 6.0 \cdot 10^5 x^{-3.1}$, $R^2 = 0.98$) estimated for the

948 pumice samples (Alfano et al 2012). The vertical axis indicates the number of particles, referred

949 to TGSD-PND, and the number of vesicles, referred to the VSD.

950 **Figure A1**. Plots showing the GSD derived for each synthetic point selected the areas Z1, Z2 and

951 Z3 (Table A1).

952 **Figure A2**. Plot showing the TGSD derived for datasets B_1, B_2 and B_3 containing 3, 9 and 15
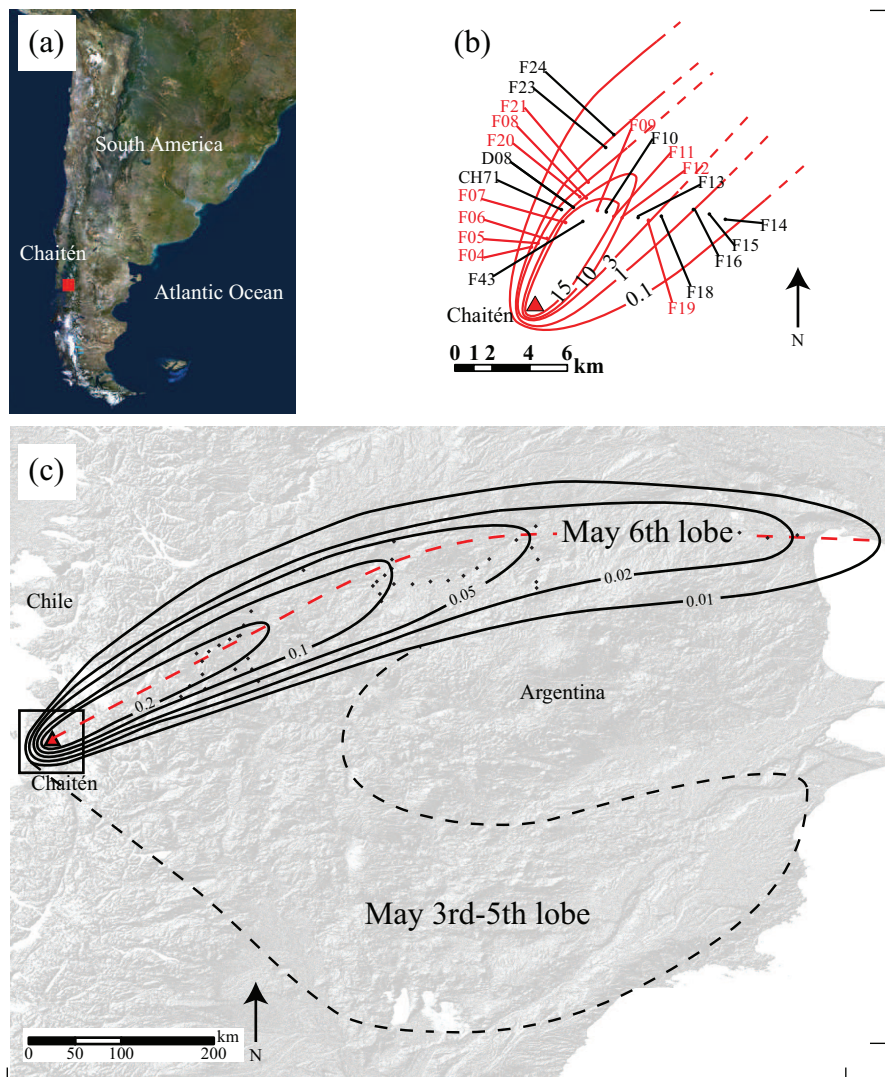
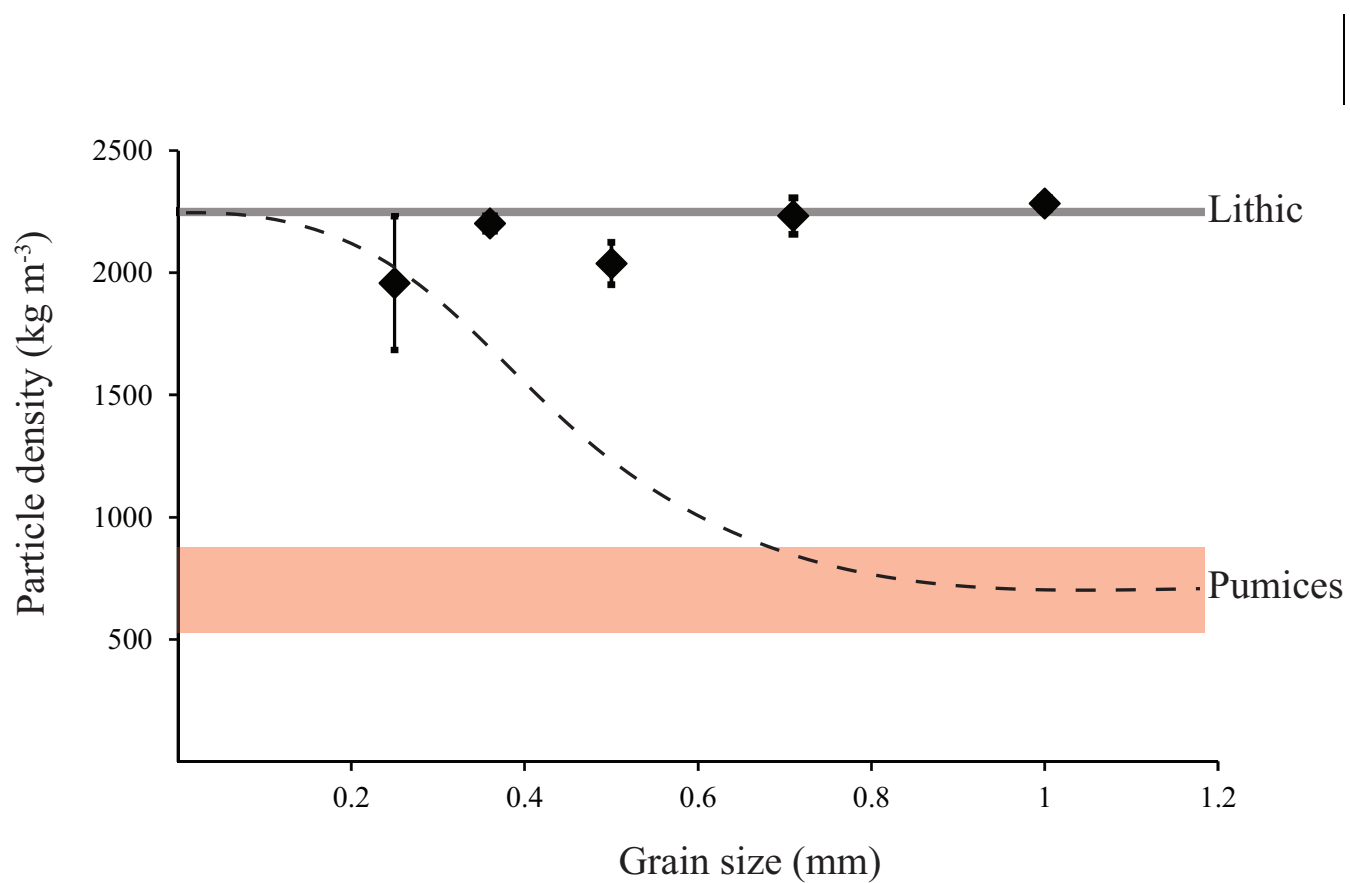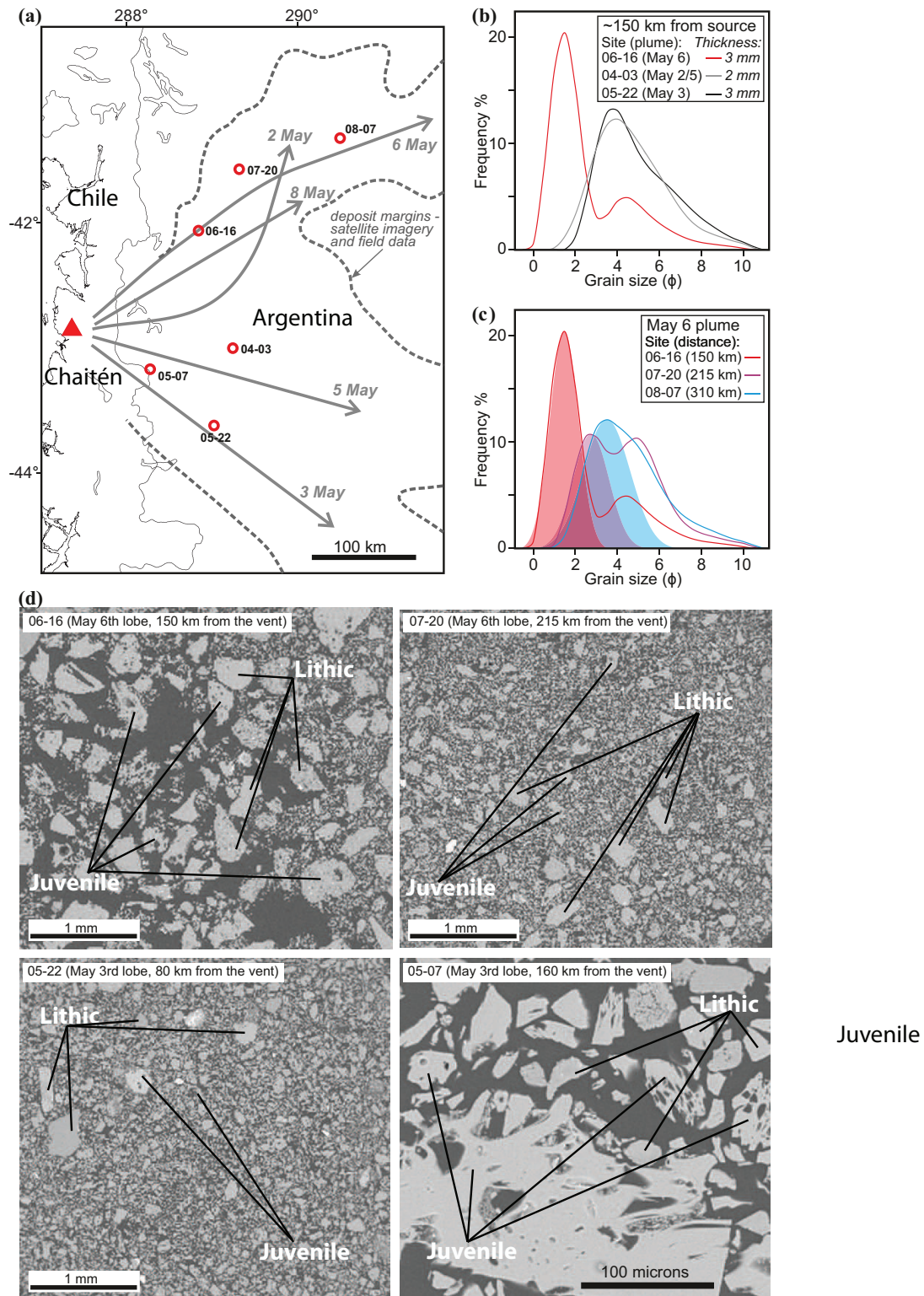953 points, respectively

954

44

Figure 1

(a)

South America

Chaitén

Atlantic Ocean

(b)

F24
F23
F21
F08
F20
D08
CH71
F07
F06
F05
F04
F43

F09
F10
F11
F12
F13
F14
F15
F16
F18
F19

15 10 5 3
0.1

Chaitén

0 1 2   4   6 km

N

(c)

Chile

May 6th lobe

0.02
0.05
0.01
0.1
0.2

Argentina

Chaitén

May 3rd-5th lobe

km
0   50 100   200   N

Figure 2

Figure 3

(a)

(b) ~150 km from source
Site (plume): *Thickness:*
06-16 (May 6) —— 3 mm
04-03 (May 2/5) —— 2 mm
05-22 (May 3) —— 3 mm

(c) May 6 plume
Site (distance):
06-16 (150 km) ——
07-20 (215 km) ——
08-07 (310 km) ——

(d)
06-16 (May 6th lobe, 150 km from the vent)
07-20 (May 6th lobe, 215 km from the vent)
05-22 (May 3rd lobe, 80 km from the vent)
05-07 (May 3rd lobe, 160 km from the vent)

Figure 4

Figure 4

Legend:
- □ Not-processed samples
- ■ (green) Pumice
- ■ (black) Obsidian
- ■ (grey) Lithic
- — Sub-populations

Panels (with Md and σ values):
- CH71: Md = -2.3, σ = 1.5
- D08: Md = -1.7, σ = 1.4
- F10: Md = -2.3, σ = 1.5
- F13: Md = -2.0, σ = 1.4
- F14: Md = 0.3, σ = 1.1
- F15: Md = 0.2, σ = 0.9
- F16: Md = 0.1, σ = 1.2
- F18: Md = -0.1, σ = 1.4
- F23: Md = 1.2, σ = 2.6
- F24: Md = -0.8, σ = 3.0
- F43: Md = -1.5, σ = 1.1
- F04: Md = -1.8, σ = 2.3
- F05: Md = -2.0, σ = 1.6
- F06: Md = -2.6, σ = 1.9
- F11: Md = -2.1, σ = 1.4
- F07: Md = -2.2, σ = 1.5
- F08: Md = -2.2, σ = 1.7
- F09: Md = -1.6, σ = 1.7
- F21: Md = -0.7, σ = 1.6
- F12: Md = -2.4, σ = 1.3
- F19: Md = -0.9, σ = 1.6
- F20: Md = -1.9, σ = 1.7

Frequency % (y-axis)

Grain size (φ) (x-axis)

Figure 5

(a)

Md_{Φ}

Distance from the vent (km)

(b)

σ_{Φ}

Md_{Φ}

Bulk sample values
- Proximal sites
× Distal sites [*Watt et al.*, 2009]

Secondary sub-populations identified in the proximal samples
- Coarse sub-population
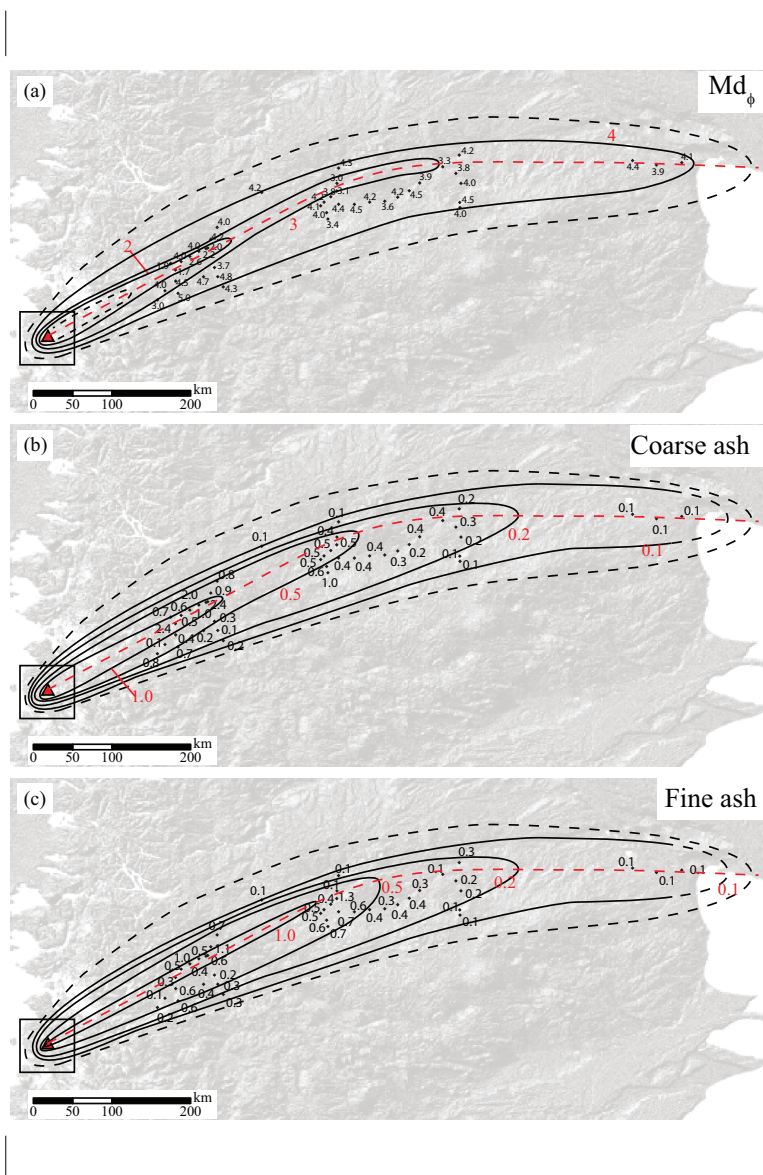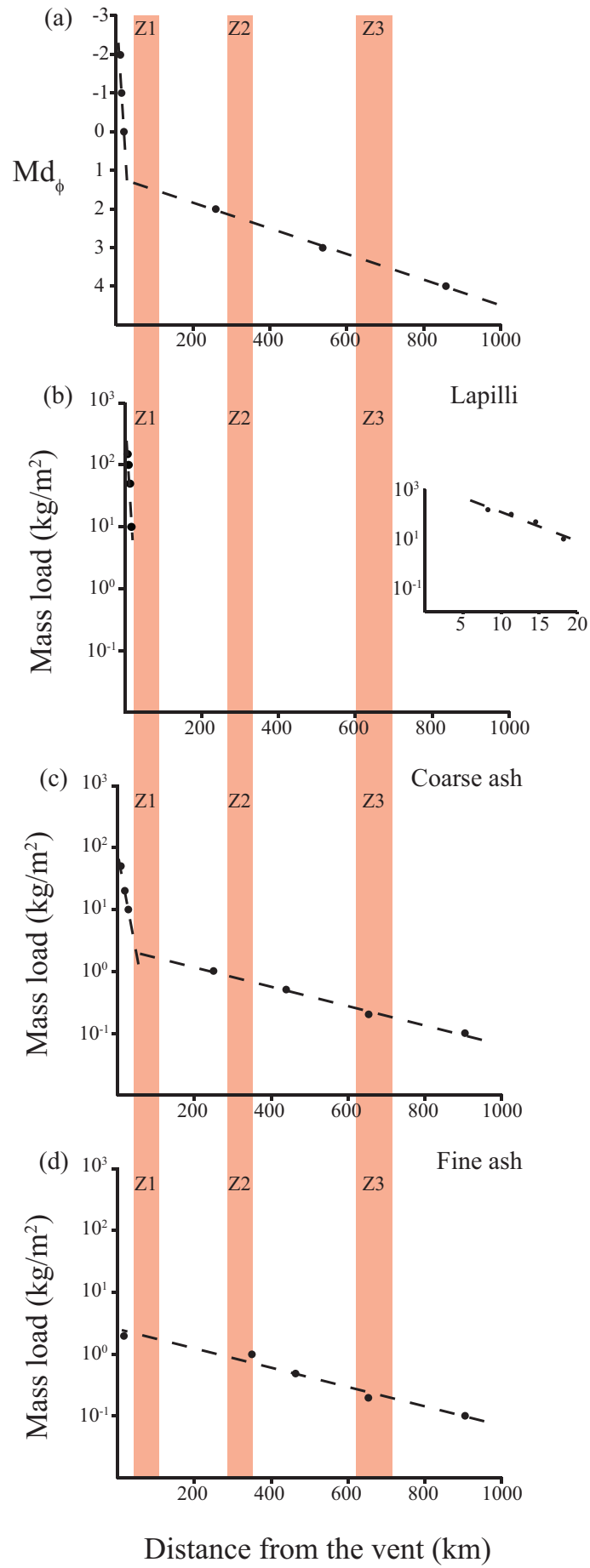- Fine sub-population

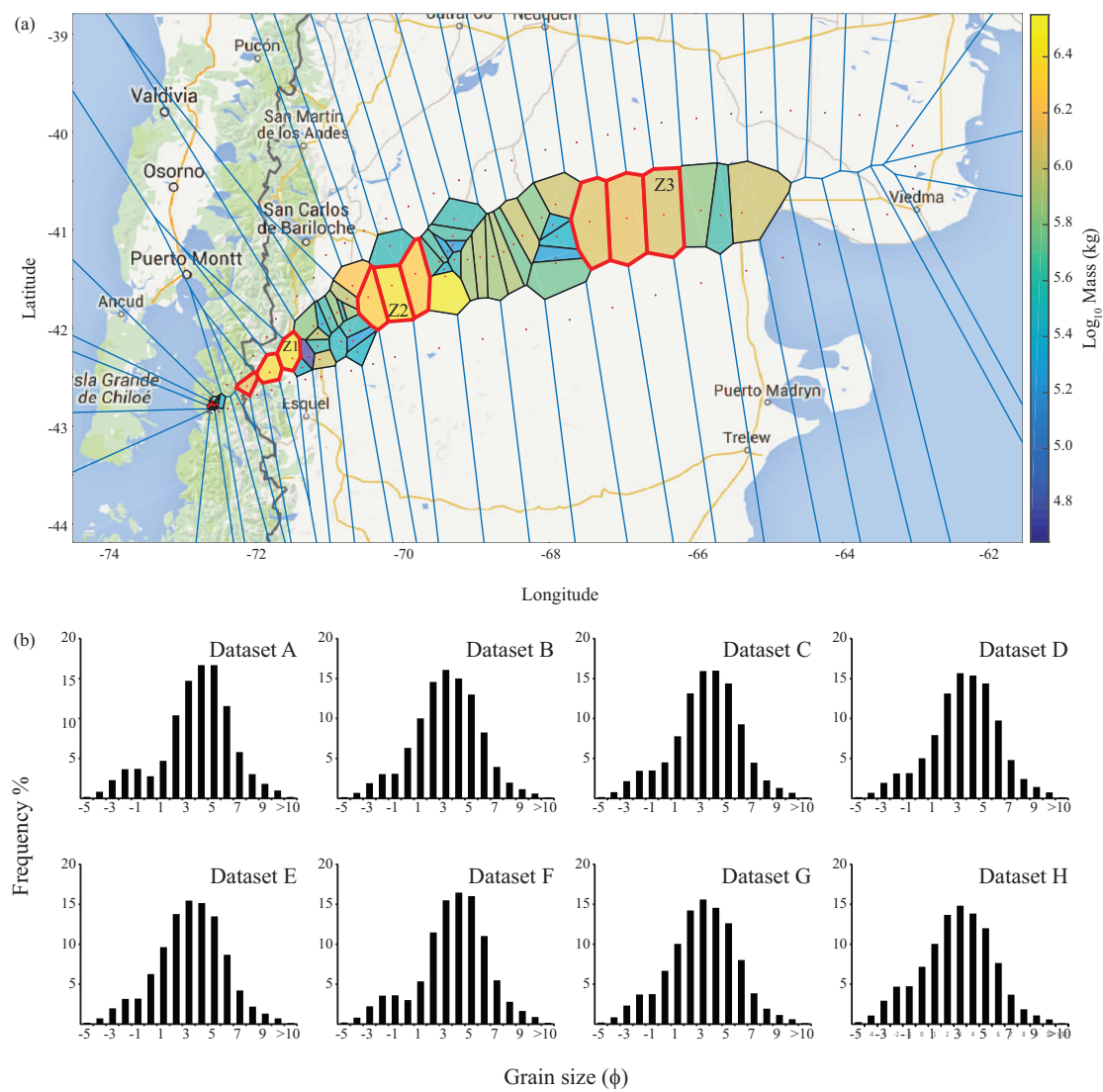Figure 6
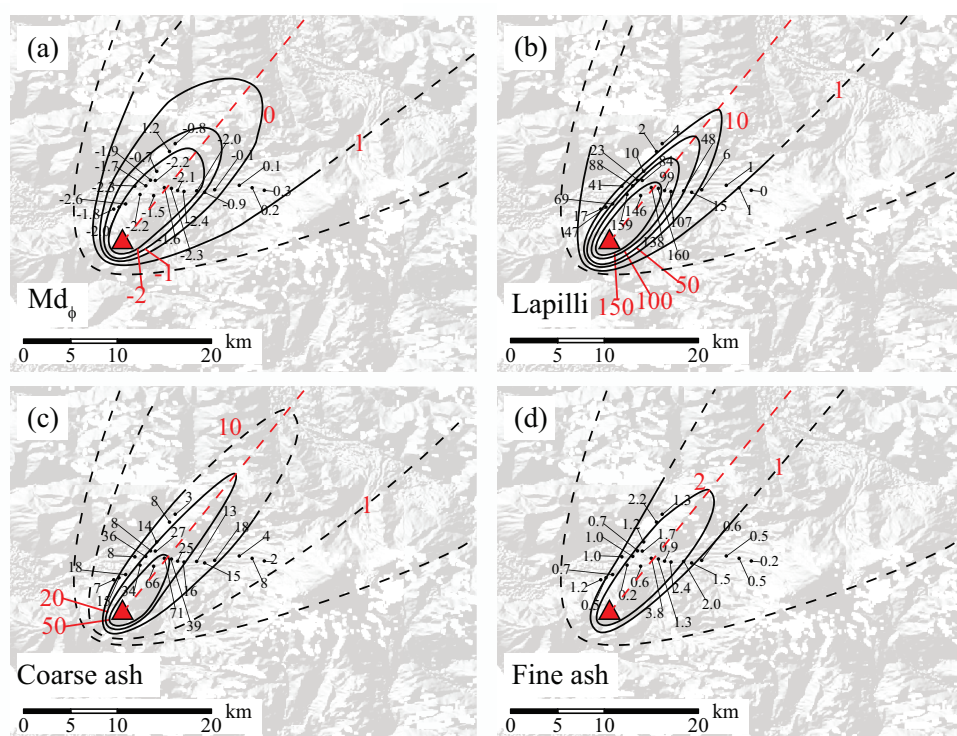
Figure 7

Figure 8

Figure 9

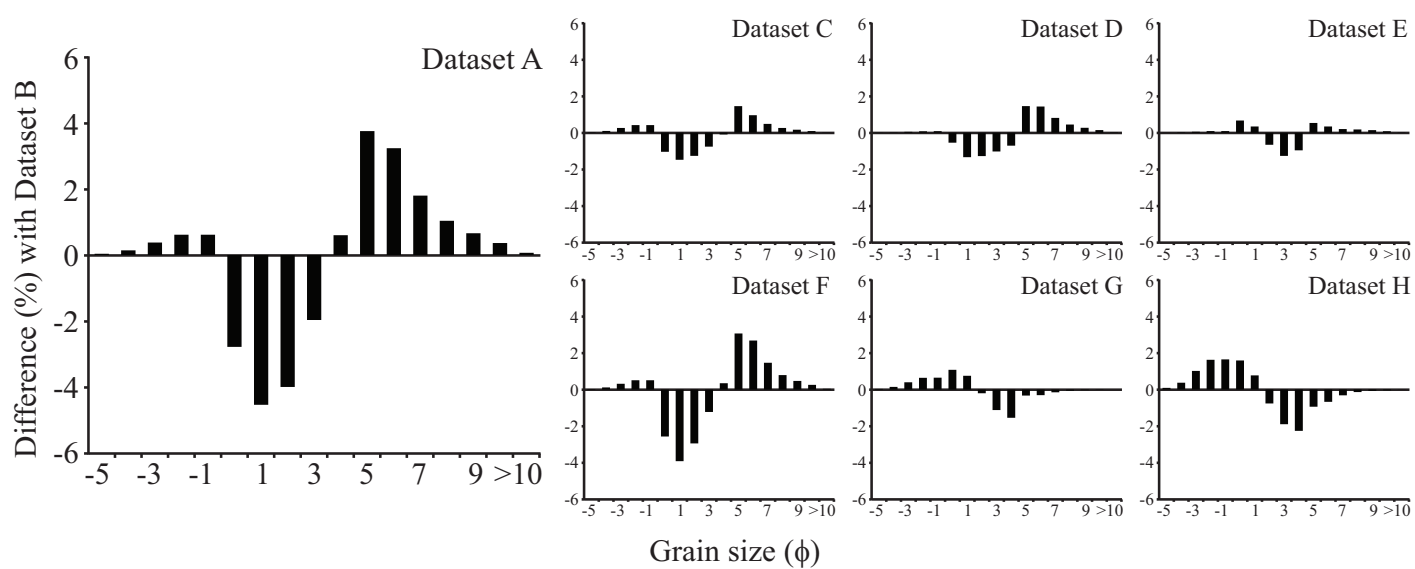
(a)

(b)

Figure 10

Grain size (φ)

Figure 11

(a)

(b)

(c)
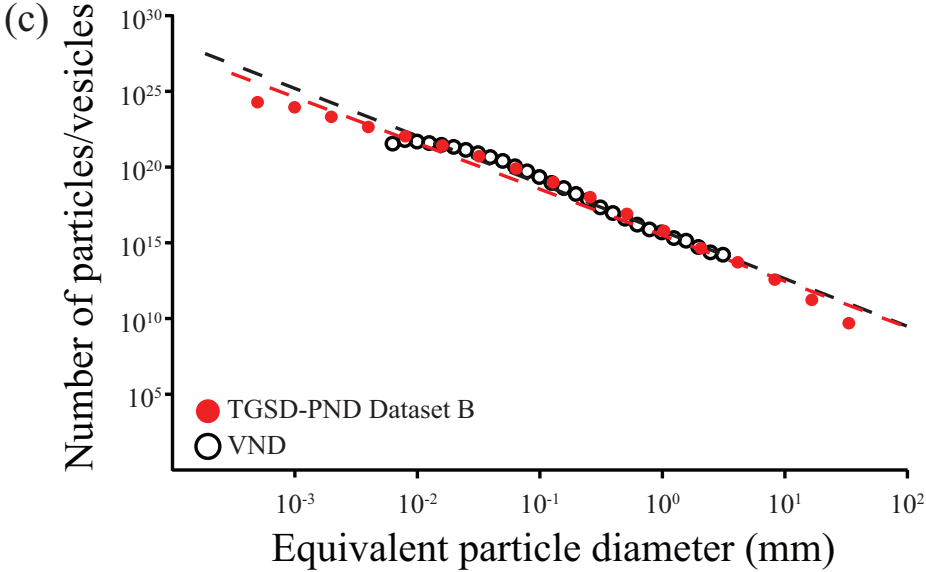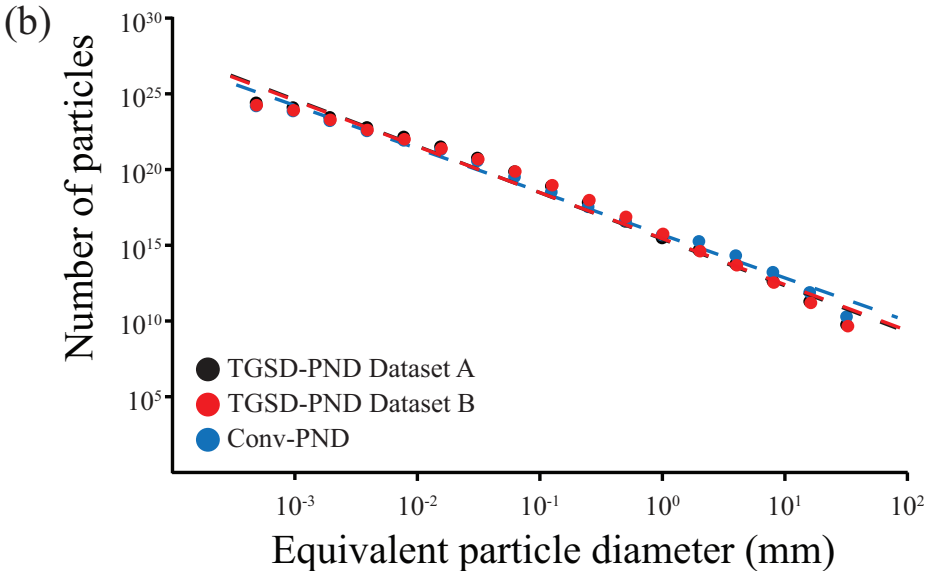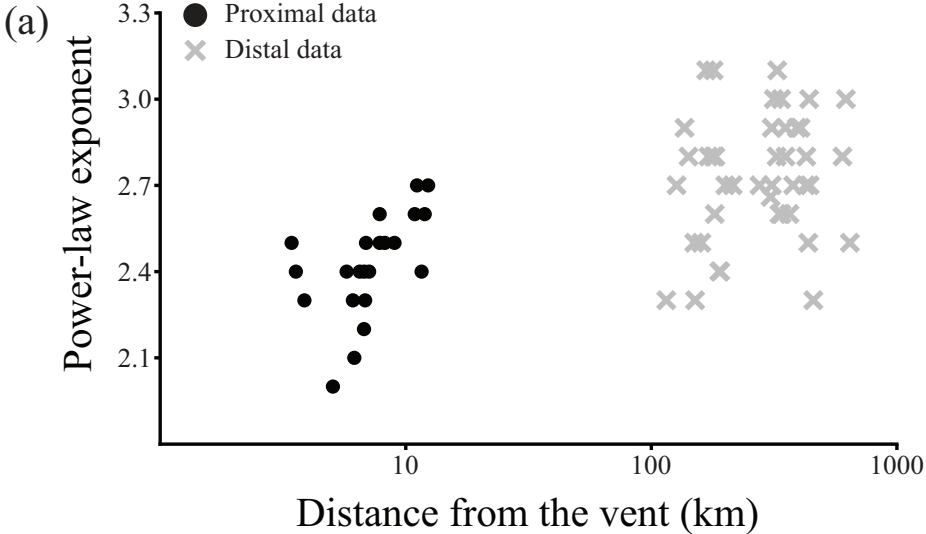
Table 1

Table 1. List and composition of the datasets used to compute the TGSD.

| Dataset	Composition
A	Includes sample data of the proximal and distal deposit and no synthetic points
B	Dataset A integrated with 9 synthetic points (3 for each gap zone)
C	Dataset A integrated with 6 synthetic points (3 for Z2 and 3 for Z3)
D	Dataset A integrated with 6 synthetic points (3 for Z1 and 3 for Z3)
E	Dataset A integrated with 6 synthetic points (3 for Z1 and 3 for Z2)
F	Dataset A integrated with 3 synthetic points for Z3
G	Dataset B with mass load of the distal points reduced to 80%
H	Dataset B with mass load of the distal points reduced to 60%
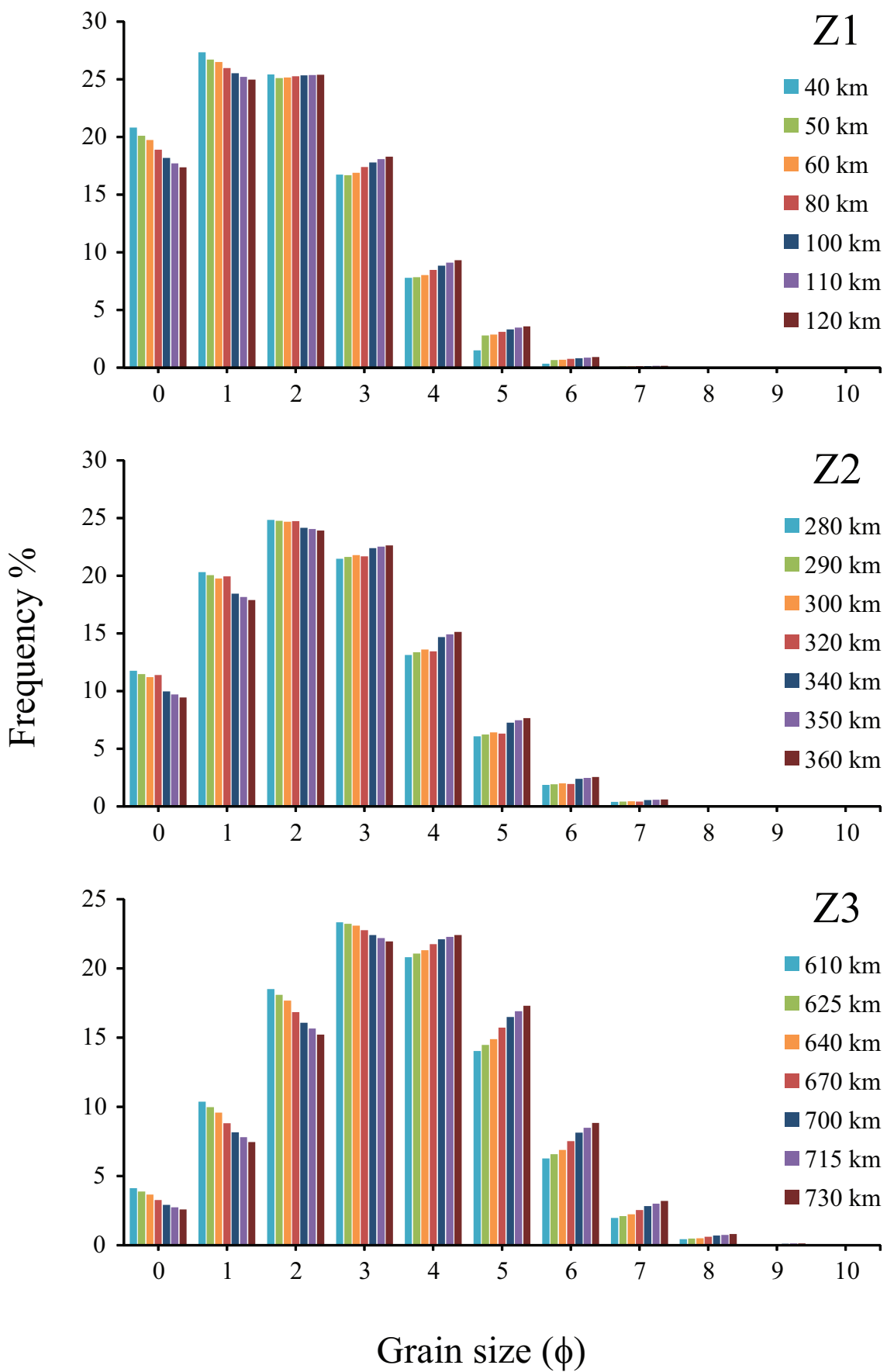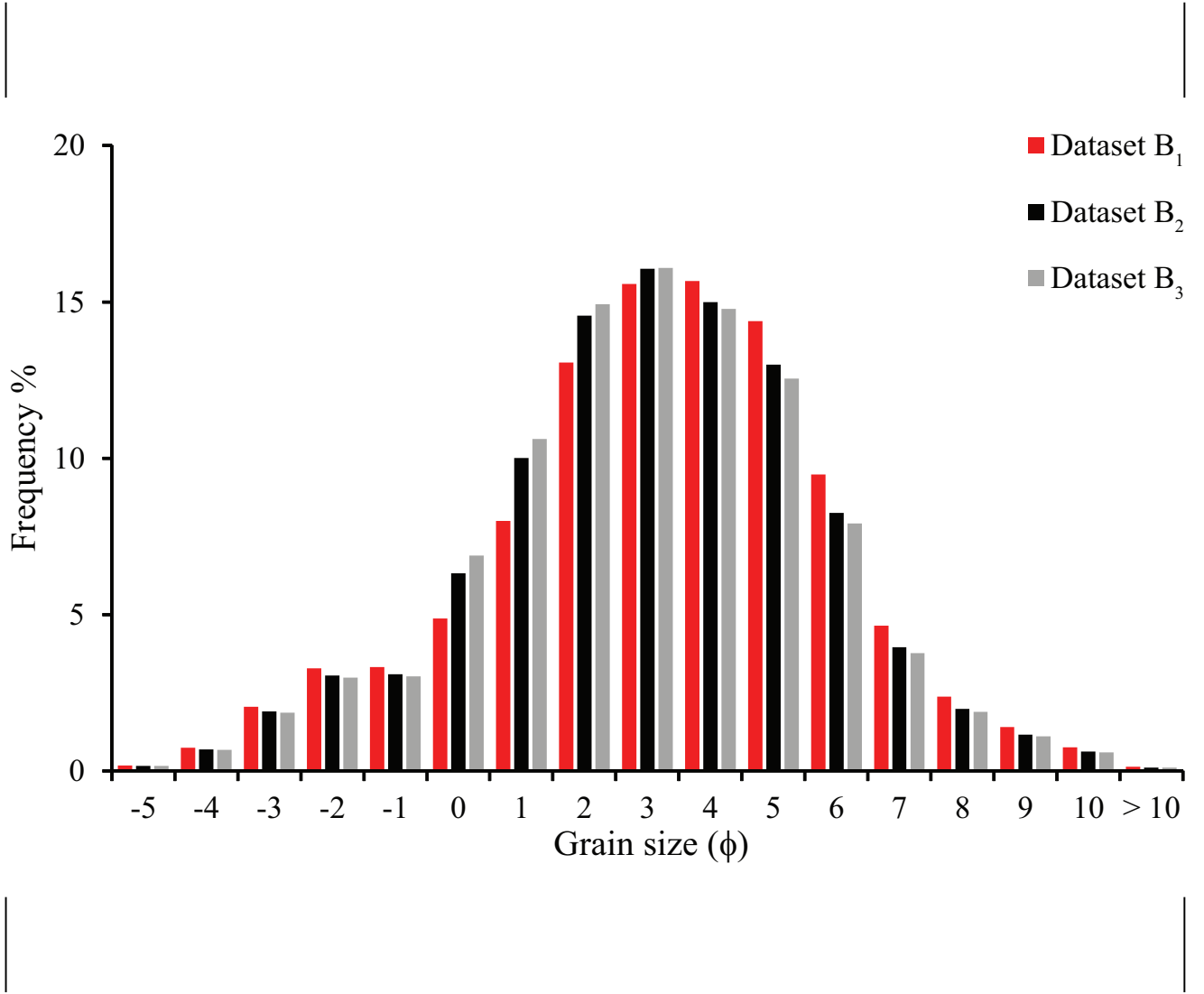
Table A1. Description of synthetic points where the distance from the vent (D, km) and values of Md_ϕ, X_c and X_f fraction, and mass load (M; kg/m^2) are reported. Z1, Z2 and Z3 indicate the 3 critical areas of Fig. 9a.

	Z1							Z2							Z3						
D	40	50	60	80	100	110	120	280	290	300	320	340	350	360	610	625	640	670	700	715	730
Md$_\phi$	1.3	1.3	1.4	1.4	1.5	1.5	1.6	2.1	2.1	2.1	2.2	2.3	2.3	2.3	3.2	3.2	3.3	3.4	3.5	3.5	3.6
X_c	3.7	1.9	1.9	1.7	1.6	1.5	1.5	0.8	0.7	0.7	0.7	0.6	0.6	0.5	0.2	0.2	0.2	0.2	0.1	0.1	0.1
X_f	2.1	2.1	2.0	1.8	1.7	1.6	1.6	0.8	0.8	0.8	0.7	0.6	0.6	0.6	0.2	0.2	0.2	0.2	0.2	0.1	0.1
M	5.9	4.0	3.8	3.5	3.3	3.1	3.0	1.6	1.5	1.5	1.4	1.3	1.2	1.2	0.4	0.4	0.4	0.3	0.3	0.3	0.3